

# Absorption, Scattering, Geodesics, Shadows and Lensing Phenomena of Black Holes in Effective Quantum Gravity

*N. Heidari*<sup>1,\*</sup>, *A. A. Araújo Filho*<sup>2,†</sup>, *R. C. Pantig*<sup>3,‡</sup>, *A. Övgün*<sup>4,§</sup>

<sup>1</sup>*Center for Theoretical Physics, Khazar University, 41 Mehseti Street, Baku, AZ-1096, Azerbaijan.*

<sup>2</sup>*Departamento de Física, Universidade Federal da Paraíba, Caixa Postal 5008, 58051-970, João Pessoa, Paraíba, Brazil.*

<sup>3</sup>*Physics Department, Mapúa University, 658 Muralla St., Intramuros, Manila 1002, Philippines.*

<sup>4</sup>*Physics Department, Eastern Mediterranean University, Famagusta, 99628 North Cyprus, via Mersin 10, Turkiye.*

March 12, 2025

## Abstract

In this work, we investigate the signatures of black holes within an effective quantum gravity framework recently proposed in the literature [1]. We begin by outlining the general setup, highlighting the two distinct models under consideration. This includes a discussion of their general properties, interpretations, and the structure of the event and inner horizons. We then examine the behavior of light in this context, analyzing geodesics, the photon sphere, and shadow formation. To validate our results, we estimate lower bounds for the shadow radius based on observational data from Sgr A\* and M87\*. Subsequently, we derive the partial radial wave equation for scalar perturbations, enabling us to study the absorption cross-section in both low- and high-frequency regimes. Additionally, we evaluate the greybody factors and provide bounds for both bosonic and fermionic fields. Finally, we present a detailed analysis of gravitational lensing in both the weak and strong deflection limits. For the weak deflection regime, the *Gauss–Bonnet* theorem is employed, while for the strong deflection limit, the *Tsukamoto* approach is utilized.

Keywords: Effective Quantum Gravity; Absorption cross-section; Greybody factor; Geodesics; Shadows; Lensing phenomena.

## Contents

<b>1</b>	<b>Introduction</b>	<b>2</b>
<b>2</b>	<b>The general setup</b>	<b>4</b>
<b>3</b>	<b>Partial wave equation</b>	<b>5</b>

---

\*E-mail: heidari.n@gmail.com (Corresponding author)

†E-mail: dilto@fisica.ufc.br

‡E-mail: rcpantig@mapua.edu.ph

§E-mail: ali.ovgun@emu.edu.tr

<b>4</b>	<b>Absorption cross-section</b>	<b>6</b>
4.1	Low-Frequency Regime . . . . .	7
4.2	High-Frequency Regime . . . . .	8
<b>5</b>	<b>Greybody factors</b>	<b>8</b>
5.1	Greybody factor for bosons . . . . .	9
5.2	Greybody factor for fermions . . . . .	10
<b>6</b>	<b>Geodesics</b>	<b>12</b>
<b>7</b>	<b>Photonspheres and shadows - an analytical consideration</b>	<b>14</b>
<b>8</b>	<b>Gravitational lensing</b>	<b>15</b>
8.1	Weak deflection limit . . . . .	16
8.1.1	Model I . . . . .	16
8.1.2	Model II . . . . .	18
8.2	Strong deflection limit . . . . .	19
8.2.1	Model I . . . . .	22
8.2.2	Model II . . . . .	23
<b>9</b>	<b>Lenses and observables</b>	<b>24</b>
9.1	Galactic phenomena: gravitational lensing by Sagittarius A* . . . . .	26
<b>10</b>	<b>Conclusion</b>	<b>27</b>

# 1 Introduction

General relativity (GR), despite its remarkable achievements, encounters several obstacles, such as the emergence of singularities [2] and its incompatibility with quantum theory [3–6]. These limitations indicate that GR may not represent the definitive description of spacetime. Consequently, ongoing research aims to extend or modify GR, often by altering one of the fundamental assumptions outlined in the Lovelock theorem, which establishes the uniqueness of Einstein’s formulation of GR [7]. In addition to various modifications discussed in the literature [8–12], this letter investigates a distinct approach that leverages the Hamiltonian formalism to construct an alternative to GR while preserving the 4-dimensional diffeomorphism invariance. Such a strategy is particularly applicable when a canonical quantum gravity framework results in a semiclassical gravity theory derived from its Hamiltonian formulation.

In GR, diffeomorphism covariance translates into the structure of the Poisson algebra when the theory is recast in its Hamiltonian formulation. However, a reverse challenge arises: determining under what circumstances a given  $3 + 1$  Hamiltonian model corresponds to a generally covariant spacetime theory. This question, first explored in works such as [13], is a fundamental concern for any effective Hamiltonian framework that emerges from a canonical approach to quantum gravity. For example, this problem has been extensively debated in the context of effective models derived from symmetry-reduced versions of loop quantum gravity [14–41].

Previous studies [19, 23, 30, 32, 34, 36, 42] have typically addressed the covariance problem by selecting a particular matter field to fix the diffeomorphism gauge. In these cases, quantization produces effective Hamiltonians that are applicable only within the chosen gauge. In contrast, a recent approach in the literature [1] has taken steps to move away from this reliance on matter field gauge fixing and aims to construct effective Hamiltonian constraints that remain consistent across different gauges. This work specifically focused on spherically symmetric vacuum gravity, establishing the

conditions for maintaining general covariance, finding the solutions that satisfy these conditions, and examining the corresponding spacetime metrics that emerge.

The field of cosmological research has greatly advanced, thanks in part to the recent detection of gravitational waves by experiments such as the LIGO–Virgo collaborations [43–45]. Gravitational waves have become indispensable for probing various cosmic phenomena, including the analysis of gravitational lensing effects within the weak–field approximation [46–51]. Historically, studies on gravitational lensing have primarily focused on light propagation over extensive distances from gravitational sources, starting with the Schwarzschild geometry [52] and later extending to more general spherically symmetric and static spacetimes [53]. However, in regions characterized by intense gravitational fields, such as those surrounding black holes, the deflection angle of light is greatly amplified, as expected in strong–field scenarios. Moreover, the deflection of light also leads to the formation of the black hole shadow, which represents one of the most striking phenomena in astrophysics, offering a direct glimpse into the warped fabric of spacetime near a black hole’s event horizon. This shadow is essentially a dark silhouette against the glowing background of hot accreting material, first theoretically predicted by James Bardeen in the 1970s as part of the Kerr metric analysis [54]. It gained prominence with the foundational work of Falcke, Melia, and Agol in 2000 [55], who proposed imaging the shadow of the supermassive black hole at the center of our galaxy, Sagittarius A\*, using Very Long Baseline Interferometry (VLBI). The observational breakthrough came in 2019 when the Event Horizon Telescope (EHT) collaboration presented the first image of a black hole shadow in the galaxy M87 and Sgr. A\*, validating key aspects of General Relativity and opening a new era in studying black hole physics, accretion processes, and testing gravity theories in extreme conditions [56–69].

The groundbreaking observations of the supermassive black hole at the center of the M87 galaxy, captured by the Event Horizon Telescope, have opened new avenues for research and drawn significant attention from the scientific community [70–75]. A key development in this area was introduced by Virbhadra and Ellis, who formulated a simplified lens equation suited for studying supermassive black holes in asymptotically flat spacetimes [76, 77]. Their findings revealed that strong gravitational lensing generates multiple symmetric images around the optical axis. Building on this, Frittelli et al. [78], Bozza et al. [79], and Tsukamoto [80] further refined the analytical tools for investigating strong–field lensing phenomena. A wide range of configurations have since been explored, including light bending in various gravitational backgrounds [77, 81–97], alternative gravity theories [46, 98–100], exotic structures such as wormholes [101–106], charged solutions like the Reissner–Nordström black hole [107–109] and rotating spacetimes [110–118]. Additionally, research on gravitational distortions and the related optical phenomena continues to expand this area of study [119, 120].

Following the solution presented in [1], several recent studies have emerged in the literature exploring various properties of the model, including gravitational lensing in both the weak [121] and strong [122] deflection regimes using Bozza’s method [123], light rings [124], quasinormal modes of the Dirac field [125], correlations between quasinormal modes and shadows [126], long-lived modes [127], and the Hod’s bound [128]. However, up to date, a comprehensive analysis that addresses geodesic trajectories, a detailed analytical study of the photon sphere and shadow structures, absorption cross–sections, scattering properties, greybody factor for scalar and Dirac perturbation, and gravitational lensing for both weak (using the *Gauss–Bonnet* theorem [129]) and strong deflection limits (through *Tsukamoto’s* technique [130]) remains absent. This work aims to fill this gap by providing a systematic investigation of these aspects, thereby contributing to a more complete understanding of the model.

## 2 The general setup

The studies discussed in [1] focus on addressing the problem of maintaining covariance within the framework of spherically symmetric vacuum gravity. By preserving the classical theory's kinematic variables and vector constraints, the authors propose an effective Hamiltonian constraint,  $H_{\text{eff}}$ , along with a freely defined function that helps build the effective metric. Similar to the classical approach, they assume the existence of a Dirac observable associated with the black hole mass. From this assumption, the authors derive conditions that ensure the preservation of spacetime covariance. These conditions reveal the interdependence of the effective Hamiltonian, the Dirac observable for the black hole mass, and the free function. Solving these conditions produces two distinct families of effective Hamiltonians, each parameterized by a quantum variable. When these quantum parameters approach zero, the classical constraints are recovered. Consequently, two distinct quantum-modified black hole metrics emerge, each corresponding to different spacetime structures.

The quantum-corrected black hole metrics are expressed by the following line element

$$ds^2 = -A(r)dt^2 + \frac{dr^2}{B(r)} + C(r)(d\theta^2 + \sin^2\theta d\phi^2). \quad (2.1)$$

Model I:

$$\begin{aligned} A(r) &= f(r) \left( 1 + \frac{\xi^2}{r^2} f(r) \right), \\ B(r) &= A(r). \end{aligned} \quad (2.2)$$

Model II:

$$\begin{aligned} A(r) &= f(r), \\ B(r) &= f(r) \left( 1 + \frac{\xi^2}{r^2} f(r) \right), \end{aligned} \quad (2.3)$$

where  $f(r) = 1 - \frac{2M}{r}$ ,  $C(r) = r^2$  and  $\xi$  is a quantum parameter, and  $M$  represents the ADM mass. The quantum parameter ( $\xi$ ) in this paper represents a fundamental component in introducing quantum gravitational corrections into the effective Hamiltonian framework. It is proportional to the Planck length ( $\ell_p = \sqrt{\hbar G/c^3}$ ) and encapsulates the microscopic effects of quantum gravity. Derived through a polymerization procedure, which replaces classical variables with trigonometric functions, the parameter models discrete space-time structures inspired by loop quantum gravity techniques. This approach ensures compatibility with quantum geometry while maintaining general covariance. Mathematically,  $\xi$  governs the oscillatory behavior of connections, such as  $\sin(\xi K)$ , effectively capturing curvature fluctuations and non-classical effects in the Hamiltonian formulation.

Physically, the scale of the quantum parameter ( $\xi$ ) aligns closely with the Planck length, approximately  $10^{-35}$  meters, indicating that its influence is dominant at microscopic distances near the black hole horizon. The effective metrics derived in the paper demonstrate that modifications proportional to  $\xi^2/x^2$  become significant in the vicinity of the horizon but diminish at larger radial distances, preserving classical general relativity at macroscopic scales. Near the event horizon, these corrections prevent singularities by introducing quantum-modified structures resembling double-horizon geometries similar to Reissner-Nordström black holes. These quantum effects also enable the smooth transitions between black and white hole regions, reinforcing the Planck-scale nature of  $\xi$  [1].

In model I, the expression for the event horizon can be found by solving  $r$  in  $A(r) = 0$ . Results give four solutions, where two are imaginary. One of the other two solutions is the horizon for the Schwarzschild case  $r_h = 2M$ , and the other one is given by the exact solution.

$$r_h = \frac{\eta^{1/3}}{3} - \frac{\xi^2}{\eta^{1/3}}, \quad (2.4)$$

where we wrote

$$\eta = 27\xi^2 M + 3\sqrt{81M^2\xi^4 + 3\xi^6}, \quad (2.5)$$

for brevity. To study the behavior of the horizon under the influence of the parameter  $\xi$ , we simplify the expression above using approximations. One of them is when  $\xi \rightarrow 0$ , Eq. (2.4) becomes

$$r_h \sim \frac{54^{\frac{1}{3}} M^{\frac{1}{3}} \xi^{\frac{2}{3}}}{3} - \frac{54^{\frac{2}{3}} \xi^{\frac{4}{3}}}{54M^{\frac{1}{3}}} + \mathcal{O}(\xi^{8/3}), \quad (2.6)$$

which shows that the horizon under the influence of  $\xi$  disappears, while the classical horizon still remains. The next approximation to Eq. (2.4) is when  $\xi \rightarrow \infty$ , which gives

$$r_h = 2M - \frac{8M^3}{\xi^2}. \quad (2.7)$$

Since the horizon derived in Eq. (2.7) is smaller than  $2M$ , it lies within the classical horizon, converging to  $2M$  as  $\xi$  becomes large, therefore Eq. (2.7) is considered as the inner horizon and thus, we adopt  $r_h = 2M$  as the event horizon. In Fig. 1, we present a numerical plot of the horizon for model I, which agrees with our analytical findings.

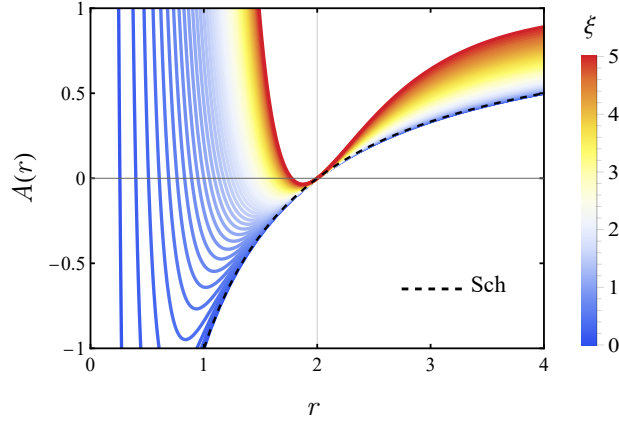


Figure 1: The lapse function of model I, for various values of  $\xi$  is represented for  $M = 1$ . The dashed line shows the Schwarzschild case

### 3 Partial wave equation

This section analyzes the partial wave equation by considering the Klein–Gordon equation in spherically symmetric curved spacetime, previously introduced in Eq. (2.2)-(2.3)

$$\frac{1}{\sqrt{-g}} \partial_\mu (\sqrt{-g} g^{\mu\nu} \partial_\nu \Psi) = 0. \quad (3.1)$$

By applying the separation of variables  $\Psi_{\omega lm}(\mathbf{r}, t) = \frac{\psi_{\omega l(r)}}{r} Y_{lm}(\theta, \varphi) e^{-i\omega t}$  [131, 132] and also defining the tortoise coordinate ( $r^*$ ) through the time and radius metric components as

$$dr^* = \frac{dr}{\sqrt{A(r)B(r)}}, \quad (3.2)$$

the Klein–Gordon equation will be simplified to a Schrödinger–like wave equation

$$\left[ \frac{d^2}{dr^{*2}} + (\omega^2 - V_{eff}) \right] \psi_{\omega l}(r) = 0. \quad (3.3)$$

Here,  $V_{eff}$  is the effective potential, given by

$$V_{eff} = A(r) \left[ \frac{l(l+1)}{r^2} + \frac{1}{r\sqrt{A(r)B(r)^{-1}}} \frac{d}{dr} \sqrt{A(r)B(r)} \right]. \quad (3.4)$$

To aid understanding, we depict  $V_{eff}$  as a function of the tortoise coordinate considering the metric parameter in Eq. (2.2) and (2.3) for Models I and II, respectively. In each plots value of the parameter  $\xi$  varies, including the Schwarzschild case ( $\xi = 0$ ) for both model I and model II, in Fig. 2.

The parameter  $\xi$  affects the effective potential's height. In both models, higher values of  $\xi$  make the height of the  $V_{eff}$  higher. However, in model 2, the effective potential is less sensitive to the variation of  $\xi$ .

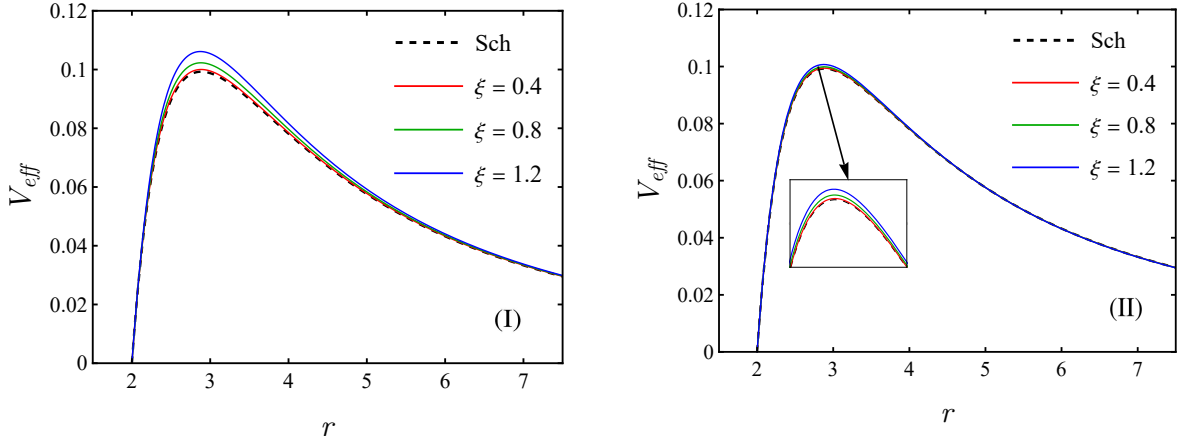


Figure 2: The effective potential is shown for  $M = 1$ ,  $l = 1$  and different values of  $\xi$ .

## 4 Absorption cross-section

As demonstrated in Fig. 2, the effective potential of the scalar field is concentrated, diminishing to zero at both the horizon and spatial infinity. Given these properties, the asymptotic behavior of the radial wavefunction is expected to be purely incoming at the event horizon, while at spatial infinity it consists of both ingoing and outgoing components. The corresponding boundary conditions are described as follows [133–135]

$$\psi_{\omega l} \approx \begin{cases} \mathcal{T}_{\omega l} R_1, & \text{for } r^* \rightarrow +r_h \ (r \rightarrow -\infty) \\ R_2 + \mathcal{R}_{\omega l} R_2^*, & \text{for } r^* \rightarrow +\infty \ (r \rightarrow \infty). \end{cases} \quad (4.1)$$

Here,  $|\mathcal{R}_l|^2$  and  $|\mathcal{T}_l|^2$  represent the reflection and transmission coefficients, respectively. Conservation of flux ensures that the relationship  $|\mathcal{R}_l|^2 + |\mathcal{T}_l|^2 = 1$  holds true. Furthermore,  $R_1$  and  $R_2$  can be expressed as [136]

$$R_1 = e^{-i\omega r^*} \sum_{j=0}^N (r - r_h)^j F_{r_h}^{(j)}, \quad (4.2)$$

$$R_2 = e^{-i\omega r^*} \sum_{j=0}^N \frac{F_{\infty}^{(j)}}{r^j}. \quad (4.3)$$

To determine the coefficients  $F_\infty^{(j)}$  and  $F_{r_h}^{(j)}$ , it is required that  $R_1$  and  $R_2$  satisfy the differential equation in Eq. (3.3) in the regions far from the black hole and near the event horizon, respectively. The phase shift,  $\delta_{\omega l}$ , is defined as [137]

$$e^{2i\delta_{\omega l}} = (-1)^{l+1} \mathcal{R}_{\omega l}. \quad (4.4)$$

To calculate the phase shifts for the absorption cross-section, we employed the numerical method discussed in Ref. [138], solving the radial equation (3.3). By using Eqs. (4.2) and (4.3) and evaluating the series up to the 10th order ( $N = 10$ ), we matched the numerical solutions to the boundary conditions in Eq. (4.1), starting near the horizon at  $r/r_h - 1 = 10^{-3}$  and extending into the asymptotically flat region at  $r \sim 200r_h$ . In this manner, the total absorption cross-section is given by  $\sigma_{abs} = \sum_{l=0}^{\infty} \sigma_{abs}^l$ , where  $\sigma_l$  is defined as [138]

$$\sigma_{abs}^l = \frac{\pi}{\omega^2} (2l + 1) (1 - |e^{2i\delta_{\omega l}}|^2). \quad (4.5)$$

Applying Eq. (4.4) and flux conservation, we get  $|e^{2i\delta_{\omega l}}|^2 = 1 - |\mathcal{R}_{\omega l}|^2 = |T_{\omega l}|^2$  [139]. Thus, the total absorption cross-section can be expressed as

$$\sigma_{abs} = \frac{\pi}{\omega^2} \sum_{l=0}^{\infty} (2l + 1) |T_{\omega l}|^2, \quad (4.6)$$

where  $|T_{\omega l}|^2$  is the transmission coefficient, also known as the greybody factor. By inserting the numerical transmission coefficients into Eq. (4.5), it can be calculated for various values of  $\xi$ . In addition, for low frequencies,  $\sigma_{abs}$  converges to the area of the black hole's event horizon, as demonstrated in previous works [140, 141].

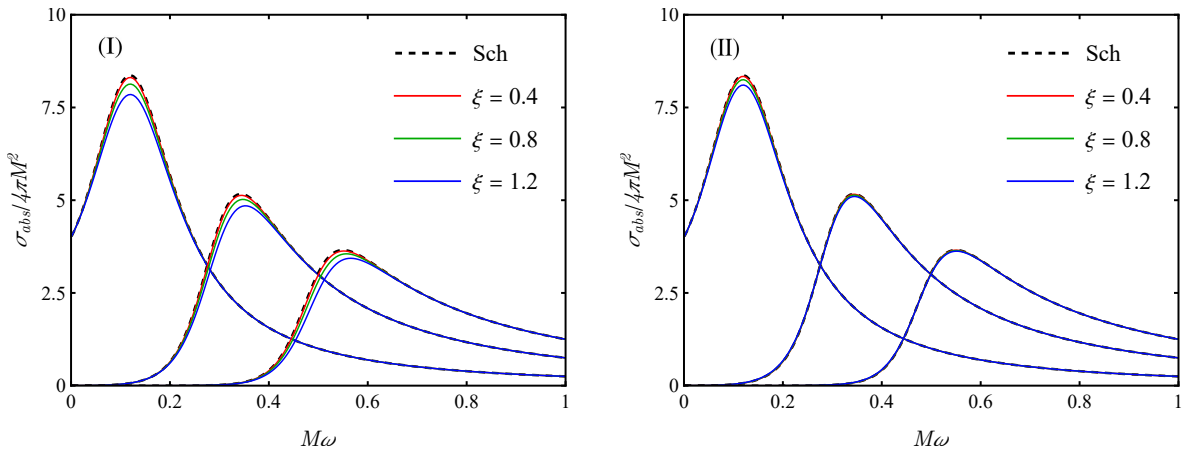


Figure 3: Partial absorption cross-sections for  $l = 0, 1, 2$  and different choices of parameter  $\xi$ .

## 4.1 Low-Frequency Regime

At low frequencies, the absorption cross-section for a black hole typically approaches the area of the event horizon. This behavior is well-documented across various studies and is a fundamental feature of black hole physics [140, 141]. As the incident wave frequency decreases, the interaction between the wave and the black hole becomes dominated by long-wavelength effects, causing the absorption cross-section to settle toward the value given by the black hole's surface area, particularly at the event horizon.

This phenomenon can be attributed to the fact that, at low frequencies, the wave's wavelength becomes comparable to or larger than the size of the black hole, leading to a simplified interaction where the cross-section reflects the fundamental size of the black hole itself. Specifically, in the case

of scalar field perturbations, the low-frequency absorption cross-section for a Schwarzschild black hole is shown to approach the geometrical area of the horizon asymptotically. This limit holds across different scenarios, including modifications in the black hole's parameters, rotating black holes, or surrounding spacetime [136, 142], as long as the frequency remains sufficiently low.

In the case of effective quantum gravity, the event horizon in both cases of Models I and II, is  $r_h = 2M$ , therefore, we expect the absorption cross-section at low-frequency regime to be  $\sigma \approx 4\pi r_h^2 = 16\pi M^2$ . We can check this parameter in Fig. 3. As expected, when frequency tends to zero,  $\sigma/4\pi M^2 \approx 4$ , which is equal to  $\sigma_{abs}$  at the event horizon.

## 4.2 High-Frequency Regime

In this section, we analyze the high-frequency limit of the absorption cross-section, also known as the geometric cross-section  $\sigma_{geo}$ . In this regard, it can be expressed as

$$\sigma_{geo} = \pi b_c^2, \quad (4.7)$$

where  $b_c$  represents the critical impact parameter for a light ray approaching the black hole. Stated differently,  $\sigma_{abs}$  of null geodesics tends to the captured cross-section in the high-frequency limit. We apply the critical impact parameter  $b_c = 3\sqrt{3}M$  for the second model and for the first model according to Eq. (7.6) and arrive at two geometric cross-section for model I and II.

$$\sigma_{geo}^I = \frac{729\pi M^4}{(27M^2 + \xi^2)}, \quad (4.8)$$

$$\sigma_{geo}^{II} = 27\pi M^2. \quad (4.9)$$

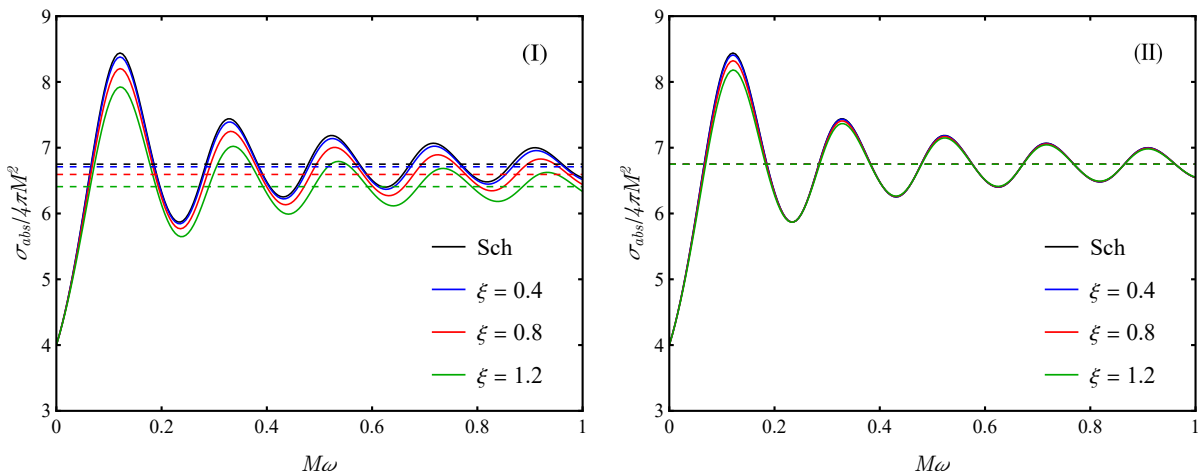


Figure 4: Total absorption cross-sections for  $l = 0$  to  $l = 6$  and different values of  $\xi$ . The dashed lines represent the geometrical cross-sections.

Fig. 4 illustrates the total absorption cross-section for  $l = 0$  to  $l = 6$  and varying  $\xi$ . In these figures, the geometric cross-section obtained via Eq. (4.7), is represented by the dashed horizontal lines. It is noticeable that in such an approximation, it converges to a constant value that is consistent with  $\sigma_{geo}$  derived in Eq. (4.8) and (4.9). In addition, in model II, the geometric cross-section does not depend on the  $\xi$ .

## 5 Greybody factors

Black holes emit radiation, known as *Hawking* radiation, due to quantum effects near the event horizon. As this radiation moves away from the event horizon, it interacts with the curved spacetime



around the black hole, resulting in changes to both the spectrum and intensity of the *Hawking* radiation reaching infinity. Thus, an observer at an infinite distance will detect it in a modified manner. The degree to which this modified spectrum deviates from a perfect black body spectrum is measured by a parameter called the greybody factor. In this section, we examine it for a massless spin-0 and spin-1/2 particles emitted from quantum-modified black holes by effective quantum gravity, using general semi-analytic estimates [143–147]. The precise bound for the greybody factor, denoted as  $T_b$ , is given by

$$T_b \geq \text{sech}^2 \left( \int_{\infty}^{+\infty} \mathcal{G} dr^* \right), \quad (5.1)$$

where

$$\mathcal{G} = \frac{\sqrt{(h')^2 + (\omega^2 - V_{eff} - h^2)^2}}{2h}. \quad (5.2)$$

Here,  $h$  is a positive function that satisfies the conditions  $h(+\infty) = h(-\infty) = \omega$ . By setting  $h$  equal to  $\omega$ , Equation (5.4) simplifies to

$$T_b \geq \text{sech}^2 \left( \int_{-\infty}^{+\infty} \frac{V_{eff}}{2\omega} dr^* \right) = \text{sech}^2 \left( \int_{r_h}^{+\infty} \frac{V_{eff}}{2\omega \sqrt{A(r)B(r)}} dr \right). \quad (5.3)$$

## 5.1 Greybody factor for bosons

In this section, we will obtain the greybody factor of the massless scalar particle with spin 0, by applying the effective potential calculated in Eq.(3.4) for both models. After substituting the effective potentials arrive at the following expressions for models I and II, respectively

$$T_b^I \geq \text{sech}^2 \left( \int_{2M}^{+\infty} \frac{r^3(2M + r\ell(\ell + 1)) - 2\xi^2(r - 4M)(r - 2M)}{r^6} dr \right), \quad (5.4)$$

and

$$T_b^{II} \geq \text{sech}^2 \left( \int_{2M}^{+\infty} \frac{\sqrt{(r - 2M)(\xi^2(r - 2M) + r^3)}}{r^8} \right. \\ \left. (r^3(2M + r\ell(\ell + 1)) - \xi^2(r - 5M)(r - 2M)) dr \right). \quad (5.5)$$

According to Eq. (5.4) and (5.5),  $\xi$  plays a significant role in the behavior of the greybody factor. In Fig. (5), we can see it is zero at very low frequencies but rises to 1 as the frequency gets higher. At lower frequencies, the wave is completely reflected by the potential barrier. However, as the frequency increases, the wave partially passes through, due to a quantum phenomenon called tunneling. When the frequency reaches a certain critical point, the reflection stops entirely. The Fig. (5) also demonstrates that the greybody factors tend to decrease with higher values of  $\xi$  which means that as  $\xi$  increases, more of the incoming wave gets scattered which is in consistency with the behavior of  $V_{eff}$  in Fig. 2. When  $\xi$  increases, the potential barrier also increases, reducing the chance of the wave being transmitted.

Although its behavior in response to an increase in the  $\xi$  values is the same in Models I and II, it is noticeable from Fig. 5 that model II is less sensitive to variations in the effective quantum gravity parameter and shows fewer changes from the usual Schwarzschild case. It is worth mentioning that a similar analysis has been accomplished in the literature in the context of other modified theories of gravity [148–153].

On the other hand, Fig. 6 represents it concerning frequency for a fixed value of  $\xi$  and different  $\ell$ . The left and right panels are devoted to model I and II, respectively. It shows that in both models the wave would be scattered less from the potential barrier when the  $\ell$  increases. However, the transmission is less sensitive to variation  $\ell$  in model I.

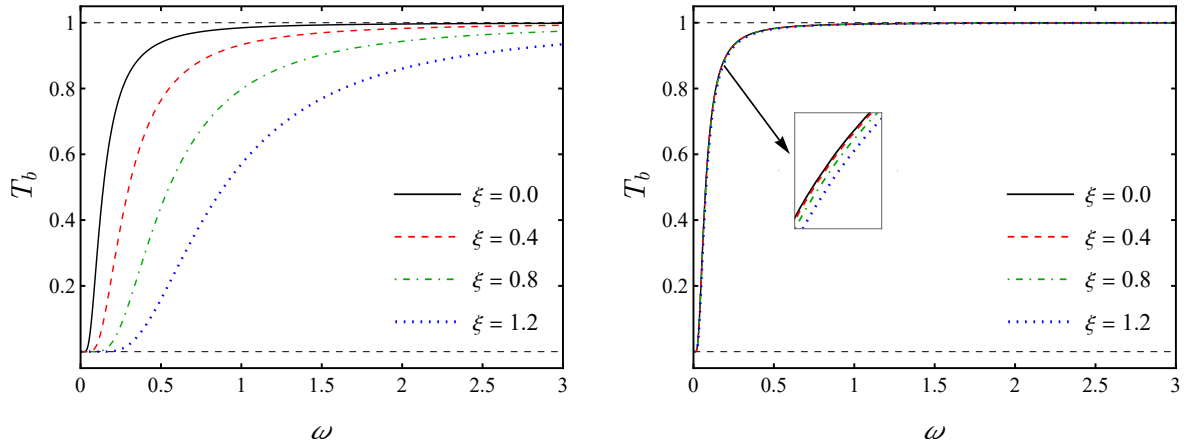


Figure 5: The analysis of the greybody factor associated with scalar fields is presented for  $M = 1$ ,  $l = 1$  alongside a range of  $\xi$  values. The left panel and right panel are allocated to model I and model II, respectively.

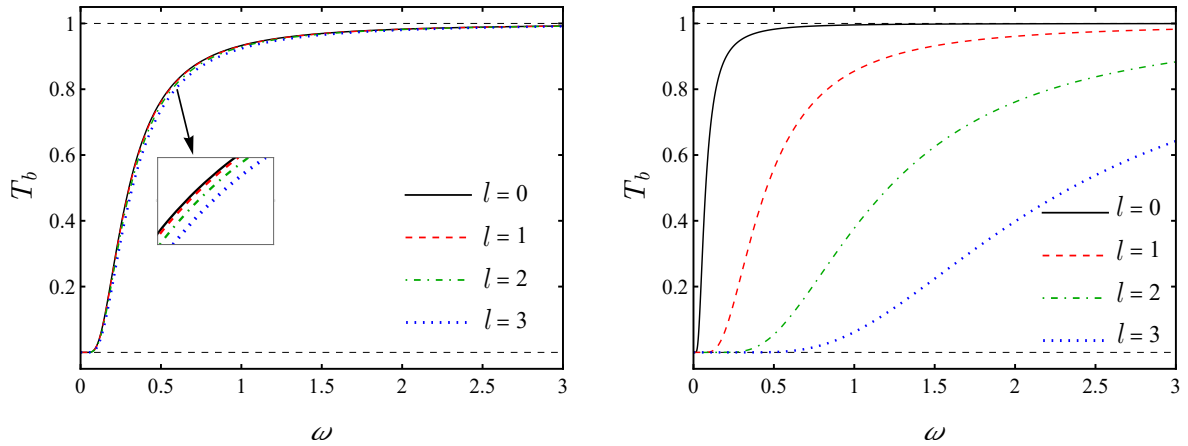


Figure 6: The comparison between greybody factor of scalar field are shown for  $M = 1$  and various values of  $l$ . The left panel and right panel are devoted to model I and II, respectively.

## 5.2 Greybody factor for fermions

In this section, we examine the massless Dirac perturbation within the context of a static, spherically symmetric black hole in effective quantum gravity spacetime. We utilize the Newman–Penrose formalism to analyze the dynamics of the massless spin-1/2 field. The Dirac equations can be expressed as follows [154, 155]

$$(D + \epsilon - \rho)F_1 + (\bar{\delta} + \pi - \alpha)F_2 = 0, \quad (5.6)$$

$$(\Delta + \mu - \gamma)F_2 + (\delta + \beta - \tau)F_1 = 0, \quad (5.7)$$

where  $F_1$  and  $F_2$  denote the Dirac spinors, with  $D = l^\mu \partial_\mu$ ,  $\Delta = n^\mu \partial_\mu$ ,  $\delta = m^\mu \partial_\mu$ , and  $\bar{\delta} = \bar{m}^\mu \partial_\mu$  representing the directional derivatives associated with the chosen null tetrad.

In this study, the appropriate null tetrad basis vectors, represented in terms of the metric elements (for simplicity  $A(r)$  and  $B(r)$  are written as  $A$  and  $B$  in the following calculations), are given by

$$l^\mu = \left( \frac{1}{A}, \sqrt{\frac{B}{A}}, 0, 0 \right), \quad n^\mu = \frac{1}{2} \left( 1, -\sqrt{AB}, 0, 0 \right), \quad (5.8)$$

$$m^\mu = \frac{1}{\sqrt{2}r} \left( 0, 0, 1, \frac{i}{\sin \theta} \right), \quad \bar{m}^\mu = \frac{1}{\sqrt{2}r} \left( 0, 0, 1, \frac{-i}{\sin \theta} \right). \quad (5.9)$$

From these definitions, we find that the non-zero components of the spin coefficients are:

$$\rho = -\frac{1}{r} \frac{B}{A}, \quad \mu = -\frac{\sqrt{AB}}{2r}, \quad \gamma = \frac{A'}{4} \sqrt{\frac{B}{A}}, \quad \beta = -\alpha = \frac{\cot \theta}{2\sqrt{2}r}. \quad (5.10)$$

A single equation of motion for  $F_1$  is derived by decoupling the equations, that describe the behavior of a massless Dirac field

$$[(D - 2\rho)(\Delta + \mu - \gamma) - (\delta + \beta)(\bar{\delta} + \beta)] F_1 = 0. \quad (5.11)$$

Substituting the expressions for the directional derivatives and spin coefficients allows us to rewrite this equation explicitly as follows

$$\left[ \frac{1}{2A} \partial_t^2 - \left( \frac{\sqrt{AB}}{2r} + \frac{A'}{4} \sqrt{\frac{B}{A}} \right) \frac{1}{A} \partial_t - \frac{\sqrt{AB}}{2} \sqrt{\frac{B}{A}} \partial_r^2 - \sqrt{\frac{B}{A}} \partial_r \left( \frac{\sqrt{AB}}{2} + \frac{A'}{4} \sqrt{\frac{B}{A}} \right) \right] F_1 + \quad (5.12)$$

$$\left[ \frac{1}{\sin^2 \theta} \partial_\phi^2 + i \frac{\cot \theta}{\sin \theta} \partial_\phi + \frac{1}{\sin \theta} \partial_\theta (\sin \theta \partial_\theta) - \frac{1}{4} \cot^2 \theta + \frac{1}{2} \right] F_1 = 0.$$

To separate the equations into radial and angular components, we assume the following form for the wave function:

$$F_1 = R(r) S_{l,m}(\theta, \phi) e^{-i\omega t}, \quad (5.13)$$

where the radial component will be formulated as follows

$$\left[ \frac{-\omega^2}{2A} - \left( \frac{\sqrt{AB}}{2r} + \frac{A'}{4} + \sqrt{\frac{B}{A}} \right) \frac{-i\omega}{A} - \frac{\sqrt{AB}}{2} \sqrt{\frac{B}{A}} \partial_r^2 - \sqrt{\frac{B}{A}} \partial_r \left( \frac{\sqrt{AB}}{2r} + \frac{A'}{4} \sqrt{\frac{B}{A}} \right) - \lambda_l \right] R(r) = 0. \quad (5.14)$$

In this case,  $\lambda_l$  serves as the separation constant. Applying the generalized tortoise coordinate  $r^*$  is defined in Eq. (3.2), the radial wave equation can be transformed into a Schrödinger-like wave equation represented as

$$\left[ \frac{d^2}{dr_*^2} + (\omega^2 - V_{eff}^\pm) \right] U_\pm = 0, \quad (5.15)$$

and the potentials  $V_{eff}^\pm$  for the massless spin-1/2 field are given by [156–158]

$$V_{eff}^\pm = \frac{(l + \frac{1}{2})^2}{r^2} A(r) \pm (l + \frac{1}{2}) \sqrt{A(r)B(r)} \partial_r \left( \frac{\sqrt{A(r)}}{r} \right). \quad (5.16)$$

We shall select this potential as  $V^+$  without any loss of generality. A similar analysis can be conducted for  $V^-$ ; since the behavior of  $V^-$  is qualitatively comparable to that of  $V^+$  [156, 159], we will focus on  $V^+$  moving forward. Now, we substitute the Dirac effective potential from Eq. (5.16) in Eq. (5.3), and the greybody factor bounds for both Models are derived. In model I, the greybody factor can be simplified to

$$T_b^I \geq \text{sech}^2 \left( \frac{1}{2\omega} \int_{2M}^{+\infty} \frac{V_{eff}^+}{\sqrt{A(r)B(r)}} dr \right) \quad (5.17)$$

$$= \text{sech}^2 \left( \frac{1}{2\omega} \int_{2M}^{+\infty} \left[ \frac{(l + \frac{1}{2})^2}{r^2} + \left( l + \frac{1}{2} \right) \partial_r \frac{\sqrt{A(r)}}{r} \right] dr \right) = \text{sech}^2 \left( \frac{(l + \frac{1}{2})^2}{4M\omega} \right). \quad (5.18)$$

From Eq. (5.17), it is notable that the result of the greybody factor does not depend on the  $\xi$  values. Therefore the influence of effective quantum gravity in Dirac perturbation of model I is not distinguishable. On the other hand, the greybody factor for model II results in

$$T_b^{II} \geq \text{sech}^2 \left( \frac{1}{2\omega} \int_{2M}^{+\infty} \frac{V_{eff}^+}{\sqrt{A(r)B(r)}} dr \right) \quad (5.19)$$

$$= \text{sech}^2 \left( \frac{1}{2\omega} \int_{2M}^{+\infty} \left[ \frac{(l + \frac{1}{2})^2}{r^2} \sqrt{\frac{A(r)}{B(r)}} + \left( l + \frac{1}{2} \right) \partial_r \frac{\sqrt{A(r)}}{r} \right] dr \right) \quad (5.20)$$

$$= \text{sech}^2 \left( \frac{1}{2\omega} \int_{2M}^{+\infty} \frac{(l + \frac{1}{2})^2}{\sqrt{r^4 + \xi^2 r(r - 2M)}} dr \right). \quad (5.21)$$

Fig. 7, the variation of the greybody factor concerning frequency is depicted. In the left panel, the behavior of greybody factor is shown for various values of  $\xi$  with fixed values of  $M = 1$  and  $l = 1$ . The plots represent that when the effective quantum gravity parameter goes higher, it increases as well, which means that more transmission occurs. In the right panel, it is shown for different angular modes  $l \geq s$ . It is noticeable that for higher  $l$ , the wavefunction is less probable to transmit.

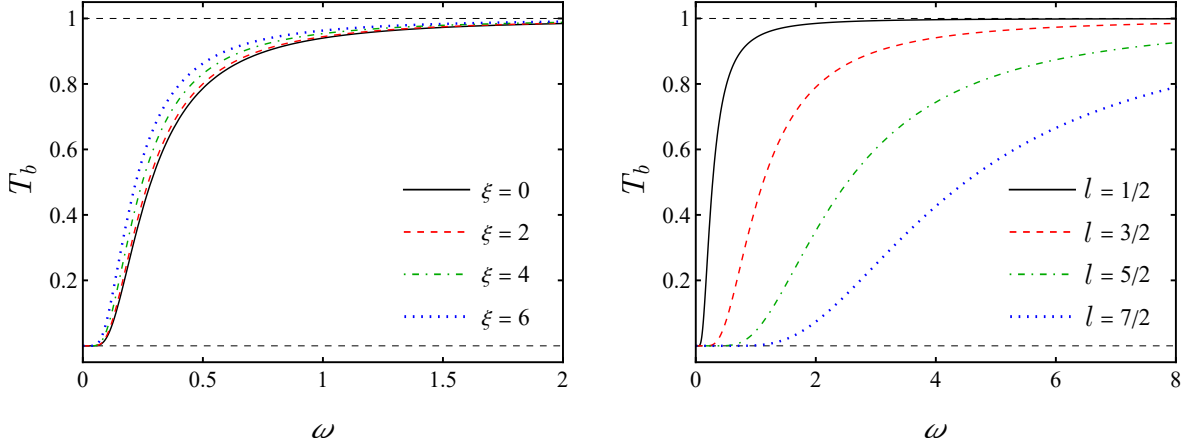


Figure 7: The greybody factor bounding of the massless Dirac field for model II: In the left panel the greybody factor is plotted for  $M = 1$ ,  $l = 1$ , and various values of  $\xi$  and in the right panel the greybody bounding is shown for  $M = 1$ ,  $\xi = 1$  and  $l = 1/2$  to  $7/2$ .

## 6 Geodesics

Geodesics play a crucial role in understanding fundamental physics, as they provide insights into spacetime curvature and describe the motion of particles in the presence of gravitational fields. Studying geodesics within the framework of effective quantum gravity has become a rapidly growing research area, focusing on how quantum corrections influence spacetime properties. By analyzing geodesics in these settings, one can better comprehend the dynamics of particles and fields at the microscopic scale, where quantum phenomena are significant. In this section, we aim to carry out a detailed exploration of geodesic behavior under such conditions. The geodesic equation is given by

$$\frac{d^2 x^\mu}{ds^2} + \Gamma_{\alpha\beta}^\mu \frac{dx^\alpha}{ds} \frac{dx^\beta}{ds} = 0, \quad (6.1)$$

with  $s$  being an arbitrary parameter. The primary objective of this analysis is to explore how the quantum gravity modification parameter  $\xi$  affects the motion of massless particles. Achieving this

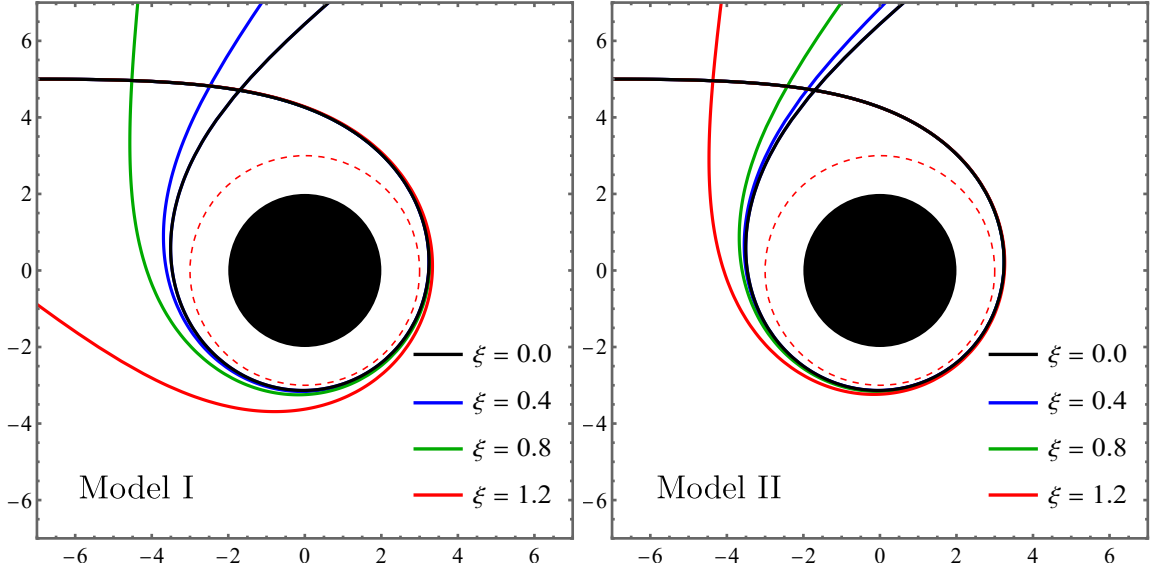


Figure 8: The geodesic trajectories are numerically calculated using  $M = 1$ ,  $b = 5$  and different values of  $\xi$  for model I. The orange dashed circle represents the photonic radius.

involves tackling a system of complex partial differential equations derived from Eq. (6.1). Specifically, the above equation produces four interdependent partial differential equations that need to be solved. Considering Eq. 2.1 - 2.3 these equations for both models are as follow

Model I:

$$\frac{dt'}{ds} = -\frac{r't'(r^3 f'(r) + 2\xi^2 r f(r) f'(r) - 2\xi^2 f(r)^2)}{r f(r) (\xi^2 f(r) + r^2)}, \quad (6.2)$$

$$\begin{aligned} \frac{dr'}{ds} = & \frac{(r')^2 (r^3 f'(r) + 2\xi^2 r f(r) f'(r) - 2\xi^2 f(r)^2)}{2r f(r) (\xi^2 f(r) + r^2)} + \\ & r (\theta')^2 \left( \frac{\xi^2 f(r)^2}{r^2} + f(r) \right) + \frac{f(r) \sin^2(\theta) (\varphi')^2 (\xi^2 f(r) + r^2)}{r}, \end{aligned} \quad (6.3)$$

Model II:

$$\frac{dt'}{ds} = -\frac{r't' f'(r)}{f(r)}, \quad (6.4)$$

$$\begin{aligned} \frac{dr'}{ds} = & -\frac{1}{2} f(r) (t')^2 \left( \frac{\xi^2 f(r)}{r^2} + 1 \right) f'(r) + \frac{(r')^2 (r^3 f'(r) + 2\xi^2 r f(r) f'(r) - 2\xi^2 f(r)^2)}{2r f(r) (\xi^2 f(r) + r^2)} + \\ & r f(r) (\theta')^2 \left( \frac{\xi^2 f(r)}{r^2} + 1 \right) + r f(r) \sin^2(\theta) (\varphi')^2 \left( \frac{\xi^2 f(r)}{r^2} + 1 \right), \end{aligned} \quad (6.5)$$

and for both models:

$$\frac{d\theta'}{ds} = \sin(\theta) \cos(\theta) (\varphi')^2 - \frac{2\theta' r'}{r}, \quad (6.6)$$

and

$$\frac{d\varphi'}{ds} = -\frac{2\varphi' (r' + r\theta' \cot(\theta))}{r}. \quad (6.7)$$

Here, the prime symbol ( $'$ ) denotes differentiation with respect to  $s$  (i.e.,  $d/ds$ ) and  $f(r) = 1 - \frac{2M}{r}$ .

Fig. 8 shows the numerically calculated geodesic paths in model I and model II, for  $M = 1$  and  $\xi = 0, 0.4, 0.8$  and  $1.2$ . The orange dashed lines indicate the photon sphere. The colored solid line indicates the path of light.

As shown in Figs. 8, light trajectories are significantly influenced by the effective quantum gravity framework in both models. Additionally, the nature of this influence differs notably between models I and II. For example, when comparing the light path for  $\xi = 1.2$  (indicated in red) in the left and right panel of Fig. 8, it becomes evident that the gravitational effects on the light in model II are more pronounced. This suggests that the quantum parameter  $\xi$  plays a crucial role in altering the gravitational lensing effect in these models, a topic that will be further explored in the following section.

## 7 Photonspheres and shadows - an analytical consideration

According to the spacetime elements in Eq. 2.1, the photon sphere can be found using the equation [160, 161]

$$A'(r)C(r) - A(r)C'(r) = 0. \quad (7.1)$$

Furthermore, due to the presence of two Killing vectors, the system has two conserved quantities: the energy, given by  $E = A(r)\dot{t}$ , and the angular momentum, expressed as  $L = C(r)\dot{\phi}$ . It is assumed that both  $E$  and  $L$  are nonzero. Using these quantities, we define the impact parameter  $b$  as follows

$$b \equiv \frac{L}{E} = \frac{C(r)\dot{\phi}}{A(r)\dot{t}}, \quad (7.2)$$

which has the following form for the photonic radius called critical impact parameter

$$b_c = \sqrt{\frac{C(r_{\text{ph}})}{A(r_{\text{ph}})}}. \quad (7.3)$$

Now, in the second model, Eq. (7.1) reduces to  $r_{\text{ph}} = 3M$ . In contrast, the first model yields four solutions, among which two are physically relevant:  $r_{\text{ph}} = 3M$ , corresponding to the standard Schwarzschild result, which remains unchanged, and

$$r_{\text{ph}} = \frac{(2\eta)^{1/3}}{3} - \frac{2\xi^2}{(2\eta)^{1/3}}. \quad (7.4)$$

Following the same approach used in the analytical analysis of the horizon, we investigate Eq. (7.4) under specific limits. When  $\xi \rightarrow 0$ , the photon sphere radius tends to zero, while the Schwarzschild case,  $r_{\text{ph}} = 3M$ , persists. In the limit  $\xi \rightarrow \infty$ , we identify that the second photon sphere is given by

$$r_{\text{ph}} = 2M - \frac{4M^3}{\xi^2}. \quad (7.5)$$

Observe that this second photon sphere coincides with the event horizon at  $2M$ . Consequently, the corresponding impact parameter is negative, indicating that this solution for  $r_{\text{ph}}$  does not contribute to shadow formation. Since the function  $A(r)$  remains unchanged from the Schwarzschild case in model II, the photon sphere radius and critical impact parameter are preserved as  $r_{\text{ph}} = 3M$  and  $b_c = 3\sqrt{3}M$ , respectively. In contrast, in model I, while the temporal component of the spacetime depends on  $\xi$ , the photon sphere radius is still  $3M$ , similar to model II. However, the impact parameter becomes  $\xi$ -dependent and is given by

$$b_c^2 = \frac{729M^4}{27M^2 + \xi^2}. \quad (7.6)$$

Then, the exact expression for the observer–dependent shadow radius is

$$R_{\text{sh}} = \sqrt{b_c^2 A(r_{\text{obs}})} = \sqrt{\frac{729M^4}{27M^2 + \xi^2} \left\{ \left(1 - \frac{2M}{r_{\text{obs}}}\right) \left[1 + \frac{\xi^2}{r_{\text{obs}}^2} \left(1 - \frac{2M}{r_{\text{obs}}}\right)\right] \right\}}. \quad (7.7)$$

We aim to reexamine and constrain the parameter  $\xi$  using the Event Horizon Telescope (EHT) observations for Sgr. A\* and M87\*. To this end, it is essential to approximate the above equation in the limit  $r_{\text{obs}} \rightarrow \infty$ . The resulting expression is given by

$$R_{\text{sh}} \sim \frac{27M^2}{\sqrt{27M^2 + \xi^2}} - \frac{27M^3}{\sqrt{27M^2 + \xi^2} r_{\text{obs}}} + \mathcal{O}(r_{\text{obs}}^{-2}). \quad (7.8)$$

Note that the first term is similar to the one that is found in Ref. [162] but without the consideration of the second term correction. To study the behavior of the shadow analytically, we again perform some approximations for  $\xi$ . When  $\xi \rightarrow 0$ , the shadow radius is given approximately as

$$R_{\text{sh}} \sim 3M\sqrt{3} - \frac{3M^2\sqrt{3}}{r_{\text{obs}}} + \left(\frac{1}{r_{\text{obs}}} - \frac{1}{M}\right) \frac{\xi^2\sqrt{3}}{18} + \mathcal{O}(\xi^4). \quad (7.9)$$

Such a result is interesting since in the weak field regime, the shadow is altered by a small value of  $\xi$ , as indicated by the third term in the above equation. This is in contrast to the strong field regime phenomena such as the horizon and the photonsphere, since if  $\xi$  is small, the classical case remains. Now, when  $\xi$  is large, we have seen deviations from the classical case for the horizon and photonsphere. But for the shadow, however,

$$R_{\text{sh}} \sim \frac{27M^2}{\xi} - \frac{27M^3}{\xi r_{\text{obs}}} - \mathcal{O}(\xi^{-3}), \quad (7.10)$$

confirming that the shadow formation vanishes. That is, one cannot detect the influence of large values of  $\xi$  in the weak field regime as far as the shadow formation is concerned. The Schwarzschild shadow radius is bounded by the following uncertainties:  $4.209M \leq R_{\text{sh}} \leq 5.560M$  for Sgr. A\* at  $2\sigma$  level of significance [163], and  $4.313M \leq R_{\text{sh}} \leq 6.079M$  for M87\* at  $1\sigma$  level of significance [164]. Let  $\delta$  represent the difference between upper (or lower) bounds and  $R_{\text{sh}}$ . Then we can calculate the constraint in the parameter  $\xi$  as

$$\xi = \pm \sqrt{-6\sqrt{3}\delta M}. \quad (7.11)$$

Results implied that there are no upper bounds for  $\xi$ , albeit negative values are also allowed. For instance, for Sgr. A\*,  $\delta = -0.987$  giving  $\xi = \pm 3.203M$ . For M87\*,  $\delta = -0.883$  leads to  $\xi = \pm 3.030M$ .

## 8 Gravitational lensing

Recently, studies have appeared in the literature employing the Bozza method to investigate gravitational lensing in the strong deflection regime [121, 121, 165] for the black hole under consideration [1]. Complementing these approaches, our work explores the lensing phenomena in the weak deflection regime using the *Gauss–Bonnet* theorem [166]. Furthermore, we extend our analysis to the strong deflection regime by utilizing the Tsukamoto technique [130]. To better organize our results, we shall present the calculations separately for model I and model II in the following subsections.

## 8.1 Weak deflection limit

### 8.1.1 Model I

This section revisits the *Gauss–Bonnet* theorem and applies it to determine the black hole’s weak deflection angle. To begin, we consider the null geodesic condition,  $ds^2 = 0$ , and manipulate it to obtain the following expression

$$dt^2 = \gamma_{ij} dx^i dx^j = \frac{1}{A(r)^2} dr^2 + \frac{r^2}{A(r)} d\Omega^2, \quad (8.1)$$

with the indices  $i$  and  $j$  span from 1 to 3, and  $\gamma_{ij}$  denotes the components of the optical metric. To apply the *Gauss–Bonnet* theorem, it becomes essential to evaluate the Gaussian curvature, which is determined as follows

$$\begin{aligned} \mathcal{K} &= \frac{R}{2} = \frac{A(r)}{2} \frac{d^2}{dr^2} A(r) - \frac{\left(\frac{d}{dr} A(r)\right)^2}{4} \\ &= \frac{6M^4 \xi^4}{r^{10}} - \frac{20M^3 \xi^4}{r^9} + \frac{24M^2 \xi^4}{r^8} - \frac{9M^3 \xi^2}{r^7} - \frac{12M \xi^4}{r^7} \\ &\quad + \frac{21M^2 \xi^2}{r^6} + \frac{2\xi^4}{r^6} - \frac{15M \xi^2}{r^5} + \frac{3M^2}{4r^4} + \frac{3\xi^2}{r^4} - \frac{M}{r^3}. \end{aligned} \quad (8.2)$$

In this context,  $\gamma$  stands for the determinant of the optical metric components  $\gamma_{ij}$ , while  $R$  denotes the Ricci scalar. The surface area confined to the equatorial plane is given by [166]:

$$dS = \sqrt{\gamma} dr d\phi = \frac{r}{A(r)^{3/2}} dr d\phi = \left[ \frac{r}{\left( \left(1 - \frac{2M}{r}\right) \left( \frac{\xi^2 (1 - \frac{2M}{r})}{r^2} + 1 \right) \right)^{3/2}} \right] dr d\phi. \quad (8.3)$$

The resulting deflection angle of light is then determined by the following expression:

$$\begin{aligned} \alpha &= - \int \int_{\bar{D}} \mathcal{K} dS = - \int_0^\pi \int_{\frac{b}{\sin \phi}}^\infty \mathcal{K} dS \\ &\simeq \frac{4M}{b} + \frac{3\pi M^2}{4b^2} + \frac{8M \xi^2}{b^3} - \frac{3\pi \xi^2}{4b^2} - \frac{45\pi M^2 \xi^2}{32b^4}. \end{aligned} \quad (8.4)$$

It should be noted that when the parameter controlling the quantum gravity corrections tends to zero ( $\xi \rightarrow 0$ ), the deflection angle converges to the classical Schwarzschild result. Fig. 9 illustrates the variation of the weak deflection angle as a function of  $b$  for different values of  $\xi$ , with the gray line indicating the Schwarzschild scenario for reference.

The expression in Eq. (8.4) can be further generalized to account for the finite distances of both the source and observer, as well as for the deflection angle of massive particles. This extension is accomplished using the approach proposed by Li et al. [167], which adapts the *Gauss–Bonnet* theorem to scenarios involving non–asymptotically flat spacetimes. Consequently, the weak deflection angle ( $\alpha_{\text{wda}}$ ) is obtained by solving:

$$\alpha_{\text{wda}} = \iint_{r_{\text{ph}}^{\text{R}} \square_{r_{\text{ph}}^{\text{S}}}^{\text{S}}} K dS + \phi_{\text{RS}} = \int_{\phi_{\text{S}}}^{\phi_{\text{R}}} \int_{r_{\text{ph}}}^{r(\phi)} K \sqrt{g} dr d\phi + \phi_{\text{RS}}. \quad (8.5)$$

The term  $\phi_{\text{RS}} = \phi_{\text{R}} - \phi_{\text{S}}$  represents the separation angle in the equatorial plane between the source and the receiver, where  $\phi_{\text{R}} = \pi - \phi_{\text{S}}$ . Here,  $K$  denotes the Gaussian curvature, expressed as

$$K = \frac{1}{\sqrt{g}} \left[ \frac{\partial}{\partial \phi} \left( \frac{\sqrt{g}}{g_{rr}} \Gamma_{rr}^\phi \right) - \frac{\partial}{\partial r} \left( \frac{\sqrt{g}}{g_{rr}} \Gamma_{r\phi}^\phi \right) \right] = -\frac{1}{\sqrt{g}} \left[ \frac{\partial}{\partial r} \left( \frac{\sqrt{g}}{g_{rr}} \Gamma_{r\phi}^\phi \right) \right]. \quad (8.6)$$



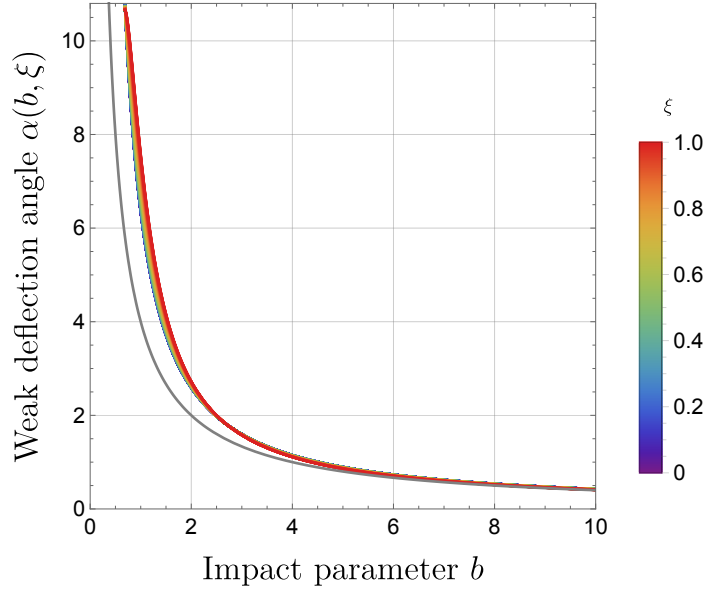


Figure 9: The deflection angle as a function of  $b$  for different values of  $\xi$  (considering a fixed value of  $M = 1$ ). The Schwarzschild case is represented by the gray line.

Given the Jacobi metric

$$dl^2 = g_{ij}dx^i dx^j = (E^2 - \mu^2 A(r)) \left( \frac{B(r)}{A(r)} dr^2 + \frac{C(r)}{A(r)} d\Phi^2 \right), \quad (8.7)$$

one can find its determinant  $g$  as

$$g = \frac{(E^2 - \mu^2 A(r))B(r)C(r)}{A(r)^2}. \quad (8.8)$$

The lower limit of the integral in Eq. (8.5) becomes zero when  $r = r_{\text{ph}}$ . Therefore, we have:

$$\int_{r_{\text{ph}}}^{r(\phi)} K \sqrt{g} dr = - \frac{A(r) (E^2 - A(r)) C' - E^2 C(r) A(r)'}{2A(r) (E^2 - A(r)) \sqrt{B(r)C(r)}} \Big|_{r=r(\phi)}, \quad (8.9)$$

where  $E$  is defined as the energy per unit mass of the particle.

To evaluate Eq. (8.9), we need the orbit equation to determine the point of closest approach to the black hole. Following standard procedures in celestial mechanics, we define  $u = r^{-1}$ . Thus, we obtain:

$$F(u) \equiv \left( \frac{du}{d\varphi} \right)^2 = \frac{C(u)^2 u^4}{A(u)B(u)} \left[ \left( \frac{E}{J} \right)^2 - A(u) \left( \frac{1}{J^2} + \frac{1}{C(u)} \right) \right], \quad (8.10)$$

where  $J = E v b$  represents the angular momentum per unit mass of the particle, with  $b$  denoting the impact parameter. The conditions  $\frac{du}{d\varphi} = \frac{d^2 u}{d\varphi^2} = 0$  must be satisfied to ensure a stable orbit. Solving the resulting differential equation under these constraints yields:

$$u(\phi) = \frac{1}{b} \sin(\phi) + \frac{M}{b^2 v^2} [1 + v^2 \cos(\phi)]. \quad (8.11)$$

To incorporate the parameter  $\xi$  into  $u(\phi)$ , we employ an iterative solution method, which results in the following expression:

$$u(\phi) = \frac{1}{b} \sin(\phi) + \frac{M}{b^2 v^2} [1 + v^2 \cos(\phi)] - \frac{\xi^2}{2v^2 b^3}. \quad (8.12)$$

Substituting this equation into Eq. (8.9), we obtain

$$\int_{r_{\text{ph}}}^{r(\phi)} K\sqrt{g} dr \sim \frac{(2E^2 - 1)M}{(E^2 - 1)b} \sin(\phi) - 1 - \frac{(3E^2 - 1)\xi^2}{b^2(2E^2 - 2)} \sin(\phi)^2 + \mathcal{O}(M\xi^2). \quad (8.13)$$

By integrating the above expression with respect to  $d\phi$ , we get

$$\begin{aligned} \int_{\phi_S}^{\phi_R} \int_{r_{\text{ph}}}^{r(\phi)} K\sqrt{g} dr d\phi &\sim -\frac{(2E^2 - 1)M}{(E^2 - 1)b} \cos(\phi) \Big|_{\phi_S}^{\phi_R} - \phi_{\text{RS}} \\ &\quad - \frac{(3E^2 - 1)\xi^2}{4b^2(E^2 - 2)} \left( \phi_{\text{RS}} - \sin(\phi) \cos(\phi) \Big|_{\phi_S}^{\phi_R} \right) + \mathcal{O}(M\xi^2). \end{aligned} \quad (8.14)$$

It is important to point out that solving for  $\phi$  is necessary in the above context. By proceeding with this, and utilizing Eq.(8.12),

$$\phi = \arcsin(bu) + \frac{M[v^2(b^2u^2 - 1) - 1]}{bv^2\sqrt{1 - b^2u^2}} + \frac{\xi^2}{2b^2v^2\sqrt{1 - b^2u^2}} + \mathcal{O}(M\xi^2). \quad (8.15)$$

For simplicity, we now assume that both the source and the receiver are equidistant from the black hole. Thus, we can set  $\phi_S = \phi$ . Under this assumption, we obtain the following expression:

$$\cos(\phi) = \sqrt{1 - b^2u^2} - \frac{Mu[v^2(b^2u^2 - 1) - 1]}{\sqrt{v^2(1 - b^2u^2)}} - \frac{u\xi^2}{2bv^2\sqrt{1 - b^2u^2}} - \mathcal{O}(M\xi^2), \quad (8.16)$$

and

$$\cos(\phi) \sin(\phi) = \sqrt{1 - b^2u^2} bu - \frac{(2b^2u^2 - 1)(b^2u^2v^2 - v^2 - 1)M}{\sqrt{1 - b^2u^2}bv^2} + \frac{(1 - 2b^2u^2)\xi^2}{2b^2v^2\sqrt{1 - b^2u^2}} - \mathcal{O}(M\xi^2). \quad (8.17)$$

By substituting Eq. (8.5) along with the two preceding equations, we derive the general formula for the weak deflection angle in model I as

$$\alpha_{\text{wda}} \sim \frac{2M(v^2 + 1)\sqrt{1 - b^2u^2}}{v^2b} - \frac{(v^2 + 2)\xi^2}{4b^2v^2} \left[ 2\sqrt{1 - b^2u^2} bu + \pi - 2 \arcsin(bu) \right] + \mathcal{O}(M\xi^2). \quad (8.18)$$

In the far-field approximation, where  $u \rightarrow 0$ , the above expression simplifies to:

$$\alpha_{\text{wda}} \sim \frac{2M(v^2 + 1)}{v^2b} - \frac{(v^2 + 2)\xi^2\pi}{4b^2v^2} + \mathcal{O}(M\xi^2). \quad (8.19)$$

Finally, for photons, where  $v = 1$ , the expression becomes

$$\alpha \sim \frac{4M}{b} - \frac{3\xi^2\pi}{4b^2} + \mathcal{O}(M\xi^2). \quad (8.20)$$

It is noteworthy that the final expression aligns with Eq. (8.4) when considering only the linear contributions, as these terms represent the dominant effects.

### 8.1.2 Model II

For the alternative model examined in this paper, the procedure to derive the weak deflection angle follows the same steps as for model I. The resulting expression is

$$\alpha_{\text{wda}} \sim \frac{2M(v^2 + 1)\sqrt{1 - b^2u^2}}{v^2b} - \frac{\xi^2 \left( 2\sqrt{1 - b^2u^2} bu + \pi - 2 \arcsin(bu) \right)}{4b^2} + \mathcal{O}(M\xi^2). \quad (8.21)$$

Here, we observe that the second term does not contain  $v$ . Thus, in the far-field approximation, it simplifies to:

$$\alpha_{\text{wda}} \sim \frac{2(v^2 + 1)M}{v^2 b} - \frac{\xi^2 \pi}{4b^2} + \mathcal{O}(M\xi^2). \quad (8.22)$$

When  $v = 1$ ,

$$\alpha_{\text{wda}} \sim \frac{4M}{b} - \frac{\xi^2 \pi}{4b^2} + \mathcal{O}(M\xi^2). \quad (8.23)$$

The key distinction between this result and that of model I is the presence of a factor of 3 in the second term.

## 8.2 Strong deflection limit

This section outlines the general approach employed to compute the deflection angle of a light ray under the strong deflection limit [130]. As in previous studies, the analysis is centered on asymptotically flat, static, and spherically symmetric spacetimes, which are described by the line element in Eq. 2.1. To utilize the method introduced by Tsukamoto [130], the metric must meet the requirement of asymptotic flatness as  $A(r)$ ,  $B(r)$ , and  $C(r)$  exhibit the following asymptotic behavior:  $\lim_{r \rightarrow \infty} A(r) = 1$ ,  $\lim_{r \rightarrow \infty} B(r) = 1$ , and  $\lim_{r \rightarrow \infty} C(r) = r^2$  which are fulfilled in the effective quantum gravity models. Additionally, due to the inherent symmetries of the spacetime, there exist two associated Killing vectors:  $\partial_t$  and  $\partial_\phi$ .

We now outline the process for determining the deflection angle in the strong field regime, beginning with the introduction of a new variable, denoted as  $D(r)$ :

$$D(r) \equiv \frac{C'(r)}{C(r)} - \frac{A'(r)}{A(r)}. \quad (8.24)$$

Here, it is important to mention that the prime symbols indicate differentiation with respect to the radial coordinate. It is assumed that the equation  $D(r) = 0$  has at least one positive root. The radius of the photon sphere, denoted by  $r_{\text{ph}}$ , corresponds to the largest positive root of  $D(r) = 0$  as discussed in Eq. 7.4. We further assume that the metric functions  $A(r)$ ,  $B(r)$ , and  $C(r)$  remain finite and positive for  $r \geq r_{\text{ph}}$ .

Owing to the axial symmetry of the system, the motion can be confined to the equatorial plane ( $\theta = \pi/2$ ). Under this condition, the radial equation simplifies to:

$$\dot{r}^2 = V(r), \quad (8.25)$$

where  $V(r) = \frac{L^2 R(r)}{B(r)C(r)}$  represents the effective potential, where  $R(r)$  is defined as  $R(r) = \frac{C(r)}{A(r)b^2} - 1$ . This equation is analogous to the motion of a particle with unit mass in a potential  $V(r)$ . The photon's trajectory is allowed wherever  $V(r) \geq 0$ . Under the asymptotic flatness conditions, we have  $\lim_{r \rightarrow \infty} V(r) = E^2 > 0$ , indicating that the photon can exist at infinity ( $r \rightarrow \infty$ ). We assume that  $R(r) = 0$  has at least one positive root.

This work focuses on a gravitational lensing scenario in which a photon, originating from infinity, travels towards a gravitational source, reaches a minimum distance of  $r_0$ , and then scatters back to infinity. For this scattering process to occur, the condition  $r_0 > r_{\text{ph}}$  must be satisfied, since closed orbits are not possible for the photon in this configuration. The distance  $r_0$  corresponds to the largest positive root of the equation  $R(r) = 0$ , where the functions  $B(r)$  and  $C(r)$  remain finite. As a result, the effective potential  $V(r)$  becomes zero at  $r = r_0$ . Given that  $r_0$  is the point of closest approach, satisfying  $R(r) = 0$ , it follows that:

$$A_0 \dot{t}_0^2 = C_0 \dot{\phi}_0^2. \quad (8.26)$$

In this context, and for the remainder of this analysis, the subscript “0” will denote quantities evaluated at  $r = r_0$ . To simplify the discussion, we can, without loss of generality, assume that

the impact parameter  $b$  is positive, particularly when considering the path of an individual light ray, defined in Eq. 7.3. It is convenient writing  $R(r)$  as

$$R(r) = \frac{A_0 C}{AC_0} - 1. \quad (8.27)$$

We establish a criterion, based on the method presented in Ref. [168], that is both necessary and sufficient for a circular light orbit to exist. Under this condition, the equation governing the trajectory is presented below

$$\frac{BC\dot{r}^2}{E^2} + b^2 = \frac{C}{A}, \quad (8.28)$$

so that

$$\ddot{r} + \frac{1}{2} \left( \frac{B'}{B} + \frac{C'}{C} \dot{r}^2 \right) = \frac{E^2 D(r)}{AB}. \quad (8.29)$$

For  $r \geq r_{\text{ph}}$ , the functions  $A(r)$ ,  $B(r)$ , and  $C(r)$  are finite and positive, along with  $E$  also being positive. The condition  $D(r) = 0$  guarantees the presence of a stable circular light orbit. Additionally, it is important to highlight that  $R'_m = \frac{D_m C_m A_m}{b^2} = 0$ , where the subscript  $m$  indicates that the respective quantities are evaluated at  $r = r_{\text{ph}}$ .

This scenario will be referred to as the strong deflection limit from this point onward. Taking the derivative of  $V(r)$  with respect to  $r$  yields

$$V'(r) = \frac{L^2}{BC} \left[ R' + \left( \frac{C'}{C} - \frac{B'}{B} \right) R \right]. \quad (8.30)$$

As  $r_0$  approaches  $r_m$  within the strong deflection limit, both  $V(r_0)$  and  $V'(r_0)$  approach zero. As a result, the equation governing the trajectory simplifies to the following form:

$$\left( \frac{dr}{d\phi} \right)^2 = \frac{R(r)C(r)}{B(r)}. \quad (8.31)$$

The deflection angle, denoted as  $\alpha(r_0)$ , is defined as

$$\alpha(r_0) = I(r_0) - \pi, \quad (8.32)$$

with, in this regard,  $I(r_0)$  reads

$$I(r_0) \equiv 2 \int_{r_0}^{\infty} \frac{dr}{\sqrt{\frac{R(r)C(r)}{B(r)}}}. \quad (8.33)$$

To continue, the first step is to address the integration process. It is worth highlighting that this step is particularly complex, as emphasized in Tsukamoto's study [130]. Furthermore, we define the following expressions, as outlined in [130]:

$$z \equiv 1 - \frac{r_0}{r}, \quad (8.34)$$

in a such way that this integral can be rewritten below

$$I(r_0) = \int_0^1 f(z, r_0) dz, \quad (8.35)$$

where

$$f(z, z_0) \equiv \frac{2r_0}{\sqrt{G(z, r_0)}}, \quad \text{and} \quad G(z, r_0) \equiv R \frac{C}{B} (1 - z)^4. \quad (8.36)$$

Additionally, when expressed in terms of  $z$ , the function  $R(r)$  takes the form:

$$R(r) = D_0 r_0 z + \left[ \frac{r_0}{2} \left( \frac{C_0''}{C_0} - \frac{A_0''}{A_0} \right) + \left( 1 - \frac{A_0' r_0}{A_0} \right) D_0 \right] r_0 z^2 + \mathcal{O}(z^3) + \dots \quad (8.37)$$

By expanding  $G(z, r_0)$  as a series in  $z$ , we obtain:

$$G(z, r_0) = \sum_{n=1}^{\infty} c_n(r_0) z^n, \quad (8.38)$$

with  $c_1(r)$  and  $c_2(r)$  being

$$c_1(r_0) = \frac{C_0 D_0 r_0}{B_0}, \quad (8.39)$$

and

$$c_2(r_0) = \frac{C_0 r_0}{B_0} \left\{ D_0 \left[ \left( D_0 - \frac{B_0'}{B_0} \right) r_0 - 3 \right] + \frac{r_0}{2} \left( \frac{C_0''}{C_0} - \frac{A_0''}{A_0} \right) \right\}. \quad (8.40)$$

Furthermore, when applying the strong deflection limit, the expression simplifies to

$$c_1(r_m) = 0, \quad \text{and} \quad c_2(r_m) = \frac{C_m r_m^2 D_m'}{2B_m}, \quad \text{with} \quad D_m' = \frac{C_m''}{C_m} - \frac{A_m''}{A_m}. \quad (8.41)$$

In shorter notation,  $G(z, r_0)$  turns out to be:

$$G_m(z) = c_2(r_m) z^2 + \mathcal{O}(z^3). \quad (8.42)$$

This indicates that the primary divergence of  $f(z, r_0)$  occurs at the  $z^{-1}$  order, leading to a logarithmic divergence in the integral  $I(r_0)$  as  $r_0$  approaches  $r_{\text{ph}}$ . To handle this divergence, the integral  $I(r_0)$  is separated into two components: a divergent term,  $I_D(r_0)$ , and a regular term,  $I_R(r_0)$ . Accordingly, the divergent portion  $I_D(r_0)$  is expressed as

$$I_D(r_0) \equiv \int_0^1 f_D(z, r_0) dz, \quad \text{with} \quad f_D(z, r_0) \equiv \frac{2r_0}{\sqrt{c_1(r_0)z + c_2(r_0)z^2}}. \quad (8.43)$$

After performing the integration, it reads

$$I_D(r_0) = \frac{4r_0}{\sqrt{c_2(r_0)}} \ln \left[ \frac{\sqrt{c_2(r_0)} + \sqrt{c_1(r_0) + c_2(r_0)}}{\sqrt{c_1(r_0)}} \right]. \quad (8.44)$$

Taking into account the series expansions of  $c_1(r_0)$  and  $b(r_0)$  around  $r_0 - r_m$ , we have:

$$c_1(r_0) = \frac{C_m r_m D_m'}{B_m} (r_0 - r_m) + \mathcal{O}((r_0 - r_m)^2), \quad (8.45)$$

and

$$b(r_0) = b_c(r_m) + \frac{1}{4} \sqrt{\frac{C_m}{A_m}} D_m' (r_0 - r_m)^2 + \mathcal{O}((r_0 - r_m)^3). \quad (8.46)$$

In other words, this leads to

$$\lim_{r_0 \rightarrow r_m} c_1(r_0) = \lim_{b \rightarrow b_c} \frac{2C_m r_m \sqrt{D_m'}}{B_m} \left( \frac{b}{b_c} - 1 \right)^{1/2}. \quad (8.47)$$

In this regards,,  $I_D(b)$  results in

$$I_D(b) = -\frac{r_m}{\sqrt{c_2(r_m)}} \ln \left[ \frac{b}{b_c} - 1 \right] + \frac{r_m}{\sqrt{c_2(r_m)}} \ln [r^2 D_m'] + \mathcal{O}[(b - b_c) \ln(b - b_c)]. \quad (8.48)$$

To proceed further, we write  $I_R(b)$  as shown below

$$I_R(b) = \int_1^0 f_R(z, b_c) dz + \mathcal{O}[(b - b_c) \ln(b - b_c)]. \quad (8.49)$$

The quantity  $f_R$  is defined as  $f_R = f(z, r_0) - f_D(z, r_0)$ . In the context of the strong deflection limit, the deflection angle can be cast as

$$a(b) = -\tilde{a} \ln \left[ \frac{b}{b_c} - 1 \right] + \tilde{b} + \mathcal{O}[(b - b_c) \ln(b - b_c)], \quad (8.50)$$

so that

$$\tilde{a} = \sqrt{\frac{2B_m A_m}{C_m'' A_m - C_m A_m''}}, \quad \text{and} \quad \tilde{b} = \tilde{a} \ln \left[ r_m^2 \left( \frac{C_m''}{C_m} - \frac{A_m''}{C_m} \right) \right] + I_R(r_m) - \pi. \quad (8.51)$$

### 8.2.1 Model I

Applying Eq. 7.6 for model I,  $\tilde{a}$  and  $\tilde{b}$  can be represented as

$$\tilde{a} = 9 \sqrt{\frac{M^2}{81M^2 + 6\xi^2}}, \quad (8.52)$$

In this context, we can express it as

$$\tilde{b} = 9 \sqrt{\frac{M^2}{81M^2 + 6\xi^2}} \ln \left( 12 - \frac{162M^2}{27M^2 + \xi^2} \right) + I_R(r_m) - \pi. \quad (8.53)$$

Unlike the situation in the Schwarzschild case, it is important to note that the contribution to the parameter  $\tilde{a}$  primarily arises from the effects of quantum gravity. Furthermore,  $I_R(r_m)$  can be computed as

$$\begin{aligned} I_R(r_m) &= \int_0^1 dz \left\{ \frac{18M}{\sqrt{-z^2(2z-3)(27M^2 + \xi^2((2z-3)z^2 + 2))}} - \frac{6M}{\sqrt{z^2 \left( 9M^2 + \frac{2\xi^2}{3} \right)}} \right\} \\ &= \frac{540M^2 \ln(3 - \sqrt{3}) + \xi^2 \left( -2\sqrt{3} + 9 - 20 \ln(6) + 20 \ln(\sqrt{3} + 3) \right)}{135M^2}. \end{aligned} \quad (8.54)$$

It is important to highlight that an analytical result was obtained when a small value of  $\xi$  was consid-

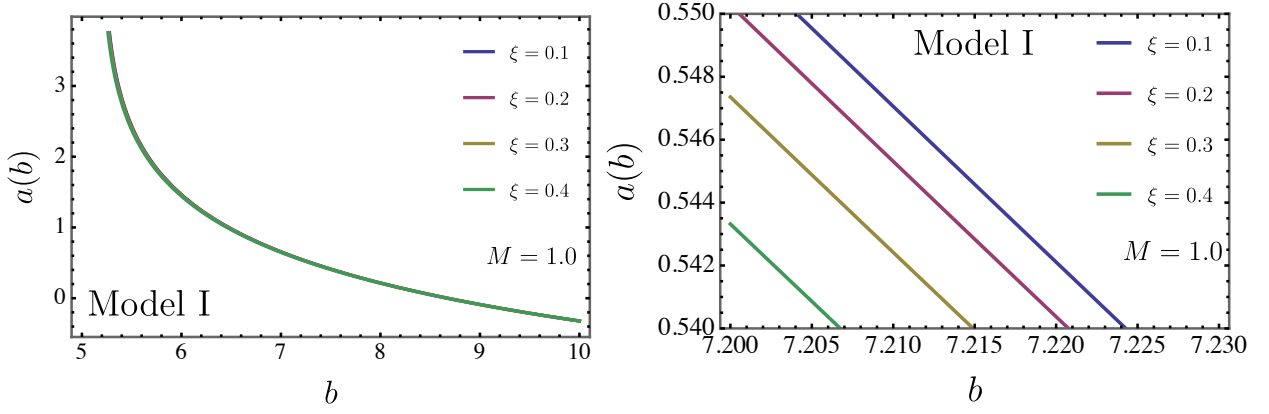


Figure 10: The strong deflection angle (Model I) as a function of  $b$  for different values of  $\xi$ .

ered. Consequently, the deflection angle given in Eq. (8.50) can be expressed as

$$\begin{aligned}
a(b) = & -9\sqrt{\frac{M^2}{81M^2 + 6\xi^2}} \ln \left[ \frac{b}{27\sqrt{\frac{M^4}{27M^2 + \xi^2}}} - 1 \right] \\
& + 9\sqrt{\frac{M^2}{81M^2 + 6\xi^2}} \ln \left( 12 - \frac{162M^2}{27M^2 + \xi^2} \right) \\
& + \frac{540M^2 \ln(3 - \sqrt{3}) + \xi^2 (-2\sqrt{3} + 9 - 20 \ln(6) + 20 \ln(\sqrt{3} + 3))}{135M^2} - \pi \\
& + \mathcal{O} \left\{ \left( b - 27\sqrt{\frac{M^4}{27M^2 + \xi^2}} \right) \ln \left[ \left( b - 27\sqrt{\frac{M^4}{27M^2 + \xi^2}} \right) \right] \right\}
\end{aligned} \tag{8.55}$$

Fig. 10 illustrates the behavior of the strong deflection angle for model I, with  $M = 1$  held constant while the parameter  $\xi$  varies. In the left panel, the influence of  $\xi$  appears minimal, as anticipated, since these variations are indicative of quantum corrections. In contrast, the right panel clearly shows that an increase in  $\xi$  corresponds to a notable decrease in the deflection angle. Lastly, the bottom panel presents the deflection angle as a function of  $M$  for a fixed  $\xi = 0.1$ , demonstrating that an increase in mass  $M$  results in a proportional increase in the deflection angle.

### 8.2.2 Model II

As mentioned in Sec. 7, the critical impact parameter is  $b_c = 3\sqrt{3}M$ , in model II. Additionally,  $\tilde{a}$  and  $\tilde{b}$  can be formulated as follows

$$\tilde{a} = 3\sqrt{3} \sqrt{\frac{M^2}{27M^2 + \xi^2}}, \tag{8.56}$$

so that

$$\tilde{b} = \ln(6) + I_R(r_m) - \pi. \tag{8.57}$$

Similarly to model I, it is important to highlight that, unlike the Schwarzschild case, the contribution to the parameter  $\tilde{a}$  primarily arises from the effective quantum gravity encoded via  $\xi$ . Further-

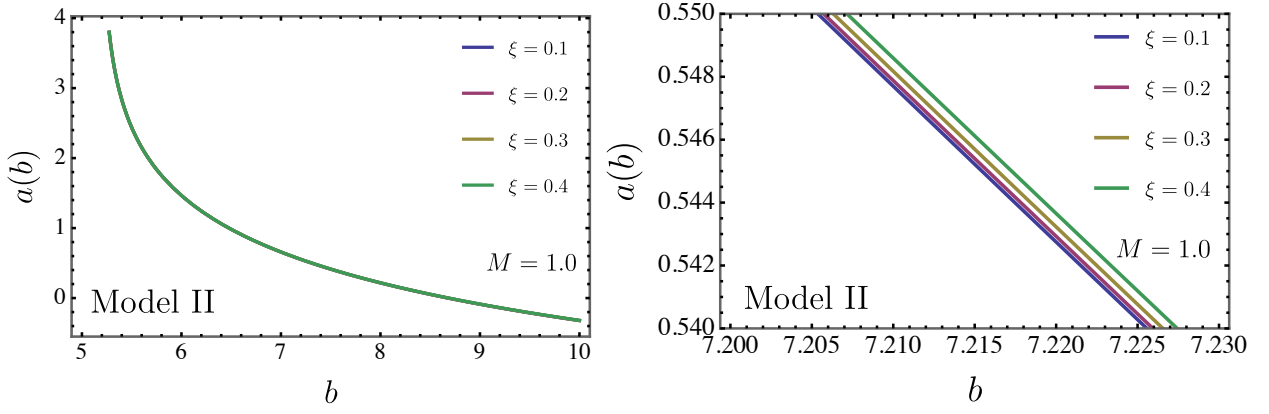


Figure 11: The strong deflection angle (Model II) as a function of  $b$  for different values of  $\xi$ .

more,  $I_R(r_m)$  can be determined as

$$\begin{aligned}
I_R(r_m) &= \int_0^1 dz \left\{ \xi^2 \left( \frac{1}{27M\sqrt{M^2z^2}} - \frac{(z-1)^2(2z+1)}{9\sqrt{3}M\sqrt{-M^2z^2(2z-3)}} \right) \right. \\
&\quad \left. + \left( \frac{2\sqrt{3}M}{\sqrt{-M^2z^2(2z-3)}} - \frac{2M}{\sqrt{M^2z^2}} \right) \right\} \\
&= \frac{540M^2 \ln(3 - \sqrt{3}) + \xi^2 \left( -2\sqrt{3} + 9 - 10 \ln(6) + 10 \ln(\sqrt{3} + 3) \right)}{135M^2}.
\end{aligned} \tag{8.58}$$

Once again, an analytical result was achieved by considering a small value of  $\xi$ . Thus, the deflection angle presented in Eq. (8.50) is expressed as

$$\begin{aligned}
a(b) &= -3\sqrt{3} \sqrt{\frac{M^2}{27M^2 + \xi^2}} \ln \left[ \frac{b}{3\sqrt{3}M} - 1 \right] + \ln(6) \\
&\quad + \frac{540M^2 \ln(3 - \sqrt{3}) + \xi^2 \left( -2\sqrt{3} + 9 - 10 \ln(6) + 10 \ln(\sqrt{3} + 3) \right)}{135M^2} - \pi \\
&\quad + \mathcal{O} \left\{ \left( b - 3\sqrt{3}M \right) \ln \left[ \left( b - 3\sqrt{3}M \right) \right] \right\}.
\end{aligned} \tag{8.59}$$

Fig. 11 depicts how the strong deflection angle varies for model II with  $M = 1$  at different values of the parameter  $\xi$ . In the left panel, the influence of  $\xi$  is minimal, which aligns with its function as a small quantum correction. Conversely, in the right panel, as  $\xi$  increases, there is a significant increase in the deflection angle. The bottom panel illustrates the deflection angle as a function of  $M$  for a fixed  $\xi = 0.1$ , indicating that a larger mass  $M$  leads to a proportionately greater deflection angle.

## 9 Lenses and observables

In this section, we will explore several parameters associated with the bending of light within strong gravitational fields, concentrating on our two models. Fig. 12 serves to illustrate the gravitational lensing phenomenon generated by the black holes outlined in this manuscript. The light emitted from the source, denoted as  $S$  (depicted as a red point), experiences deflection as it moves toward the observer, labeled  $O$  (shown as a purple point), due to the gravitational influence of the black holes located at point  $L$  (represented by an orange point). Moreover, point  $I$  (highlighted in blue) indicates the image seen by observer  $O$ . The angular positions of both the source and the observed image are



designated as  $\beta$  and  $\theta$ , respectively. The angular deviation, represented by  $a$ , measures the alteration in the light's trajectory as it passes through the gravitational field.

Additionally, we utilize the same configuration outlined in [169], where we consider that the source ( $S$ ) is nearly perfectly aligned with the lens ( $L$ ). This particular setup is significant due to the emergence of relativistic images. In this context, the lens equation that describes the relationship between  $\theta$  and  $\beta$  can be formulated as

$$\beta = \theta - \frac{D_{LS}}{D_{OS}} \Delta a_n. \quad (9.1)$$

In this context,  $\Delta a_n$  denotes the deflection angle that incorporates all the loops made by the photons before arriving at the observer, specifically defined by  $\Delta a_n = a - 2n\pi$ . Within this approach, we utilize the approximation for the impact parameter as follows  $\tilde{b} \simeq \theta D_{OL}$ . As a result, the angular deviation can be expressed as

$$a(\theta) = -\tilde{a} \ln \left( \frac{\theta D_{OL}}{b_c} - 1 \right) + \tilde{b}. \quad (9.2)$$

To obtain  $\Delta a_n$ , we perform an expansion of  $a(\theta)$  around  $\theta = \theta_n^0$ , where the condition  $\alpha(\theta_n^0) = 2n\pi$  is satisfied

$$\Delta a_n = \left. \frac{\partial a}{\partial \theta} \right|_{\theta=\theta_n^0} (\theta - \theta_n^0). \quad (9.3)$$

Considering Eq. (9.2) at  $\theta = \theta_n^0$ , we derive

$$\theta_n^0 = \frac{b_c}{D_{OL}} (1 + e_n), \quad \text{where } e_n = e^{\tilde{b} - 2n\pi}. \quad (9.4)$$

By inserting (9.4) into (9.3), we derive  $\Delta a_n = -\frac{\tilde{a} D_{OL}}{b_c e_n} (\theta - \theta_n^0)$ . When we subsequently integrate this result into the lens equation (9.1), we can formulate the expression for the  $n^{\text{th}}$  angular position of the image

$$\theta_n \simeq \theta_n^0 + \frac{b_c e_n}{\tilde{a}} \frac{D_{OS}}{D_{OL} D_{LS}} (\beta - \theta_n^0). \quad (9.5)$$

Although the deflection of light preserves surface brightness, the presence of the gravitational lens alters the solid angle of the source, affecting its visual representation. The total flux received

from a relativistic image is related to the magnification  $\mu_n$ , which is defined as  $\mu_n = \left| \frac{\beta}{\theta} \frac{\partial \beta}{\partial \theta} \right|_{\theta_n^0}^{-1}$ . By applying (9.1) and noting that  $\Delta a_n = -\frac{\tilde{a} D_{OL}}{b_c e_n} (\theta - \theta_n^0)$ , we derive

$$\mu_n = \frac{e_n (1 + e_n)}{\tilde{a} \beta} \frac{D_{OS}}{D_{LS}} \left( \frac{b_c}{D_{OL}} \right)^2. \quad (9.6)$$

It is important to note that the magnification factor  $\mu_n$  rises with increasing  $n$ . As a result, the brightness from the initial image  $\theta_1$  greatly exceeds that of the later images. However, the total luminosity remains relatively low, largely because of the term  $\left( \frac{b_c}{D_{OL}} \right)^2$ . Additionally, a significant aspect is the occurrence of magnification divergence as  $\beta$  approaches zero, highlighting that optimal alignment between the source and the lens enhances the likelihood of observing relativistic images.

In essence, we have detailed the positions and fluxes of relativistic images based on the expansion coefficients ( $\tilde{a}$ ,  $\tilde{b}$ , and  $b_c$ ). By redirecting our attention to the inverse problem, we seek to extract these expansion coefficients from observational data. This endeavor not only enhances our understanding of the characteristics of the object causing the gravitational lensing effect but also allows for meaningful comparisons with predictions made by modified theories of gravity.

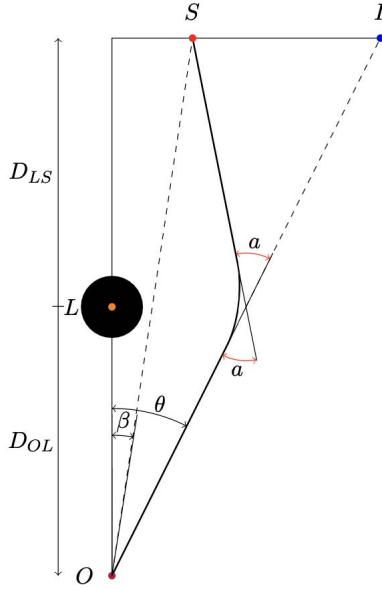


Figure 12: Depiction of gravitational lensing: light emitted from the source  $S$  (represented by the red point) is deflected as it travels towards the observer  $O$  (indicated by the purple point) due to the gravitational influence of a compact object located at  $L$  (shown as the orange point). The observer  $O$  perceives the resulting image at  $I$  (marked in blue). The distance between the lens  $L$  and the observer  $O$  is denoted as  $D_{OL}$ , while  $D_{LS}$  represents the distance from the source's projected position to the lens along the optical axis. The large black dot symbolizes the black hole being analyzed [170]

Furthermore, the impact parameter can be related to  $\theta_\infty$ , as outlined in [169]

$$b_c = D_{OL}\theta_\infty, \quad (9.7)$$

where  $\theta_\infty$  refers to the additional relativistic images. We will adopt Bozza's approach, as described in [169], which treats only the outermost image  $\theta_1$  as a separate entity, while the other images are included within  $\theta_\infty$ . To provide further clarification, Bozza proposed the following observables:

$$s = \theta_1 - \theta_\infty = \theta_\infty e^{\frac{\tilde{b}-2\pi}{\tilde{a}}}, \quad (9.8)$$

$$\tilde{r} = \frac{\mu_1}{\sum_{n=2}^{\infty} \mu_n} = e^{\frac{2\pi}{\tilde{a}}}. \quad (9.9)$$

In these expressions,  $s$  indicates the angular separation, while  $\tilde{r}$  defines the ratio of the flux from the primary image to the total flux of all remaining images. These relationships can be inverted to extract the expansion coefficients. In the following subsection, we will analyze a concrete astrophysical scenario to compute these observables and assess the impact of the effective quantum gravity parameter,  $\xi$ , on these values.

## 9.1 Galactic phenomena: gravitational lensing by Sagittarius A\*

Observational data on stellar dynamics provide strong evidence for a compact, enigmatic object residing at the center of our galaxy. This object, identified as the supermassive black hole Sagittarius (Sgr) A\*, is estimated to have a mass of around  $4.4 \times 10^6 M_\odot$  [171]. To gain further insight into this astronomical entity, we investigate its characteristics using the parameter  $\xi$ , which allows us to study the behavior of key observables associated with this phenomenon. To compute these observables, we assume a distance of  $D_{OL} = 8.5$  Kpc. Using the critical impact parameters  $b_c = 27\sqrt{\frac{M^4}{27M^2 + \xi^2}}$  and

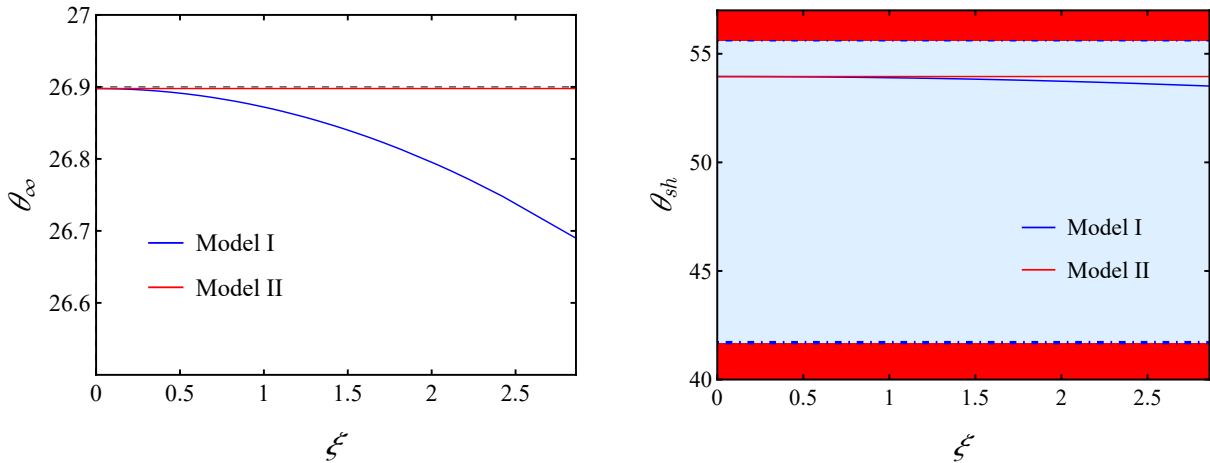


Figure 13: The left panel represents the behavior of lensing observables ( $\theta_\infty$ ) by changing with quantum effective potential parameter  $\xi$  for Sagittarius A\*. The black dashed corresponds to Sagittarius A\* as a Schwarzschild case. The right panel shows the shadow angular diameter  $\theta_{\text{sh}}$  as a function of  $\xi$ , considering the constraints observed by Sgr A\*.

$b_c = 3\sqrt{3}M$  for model I and model II respectively, we arrive at the following form for  $\theta_\infty$  based on Eq. 9.7

$$\theta_\infty^I = 614.965 \sqrt{\frac{1}{\xi^2 + 522.72}} \approx 26.8977 - 0.0257286\xi^2 + O(\xi^4), \quad (9.10)$$

$$\theta_\infty^{II} \approx 26.8977.$$

In Fig. 13, the behaviour of observable,  $\theta_\infty$  with variation of  $\xi$ , is shown in the left panel. It can be observed that in model I, the angular position, slightly deviates from the result obtained for the Schwarzschild black hole. However, it matches the value obtained for the Schwarzschild black hole in model II due to the point that the impact parameter has the same value as the Schwarzschild case. Moreover the shadow angular diameters  $\theta_{\text{sh}} = 2\theta_\infty$  are represented in the right panel. Also the  $1\sigma$  constraints of Sgr. A\* determined the allowed range of angular shadow diameter as  $41.7 < \theta_{\text{sh}} < 55.6$  ( $\mu\text{as}$ ) according to ref. [172]. Therefore there isn't any constraint on the effective quantum gravity parameter based on the right panel plots, and angular shadow diameter lies in the allowed range for both models.

## 10 Conclusion

In this study, we investigated the implications of black holes within the framework of effective quantum gravity as proposed by Ref. [1]. First, we analyzed the behavior of the lapse function and the structure of the horizons. The trajectories of light in the spacetimes of Models I and II were numerically simulated for various values of  $\xi$ . Additionally, we examined wave-like phenomena using a test scalar field and computed the absorption cross-section through partial wave analysis for both models. Our findings revealed that, in both cases, the effective quantum gravity parameter  $\xi$  impacted the partial and total absorption cross-sections, with higher values of  $\xi$  leading to lower absorption as observed by a distant detector. However, model II showed a reduced sensitivity to variations in  $\xi$ . We also demonstrated that at low frequencies, the total absorption cross-section approached the black hole's horizon area, while at higher frequencies, it converged with the capture cross-section for null geodesics, as predicted by partial wave analysis.

We further explored the greybody factor bounds for scalar and Dirac perturbations. For scalar fields in both models, we found that the greybody factor decreased as  $\xi$  increased, suggesting that

stronger effective quantum gravity reduces the probability of wave penetration through the black hole's potential barrier. In contrast, for the Dirac field, the greybody factor in model I remained unaffected by changes in  $\xi$ , whereas in model II, it tended to decrease as  $\xi$  increased.

Finally, we carried out a comprehensive analysis of gravitational lensing under both weak and strong deflection limits. For the weak deflection regime, the *Gauss–Bonnet* theorem was applied, whereas the *Tsukamoto* method was utilized for the strong deflection limit. Additionally, we derived the corresponding observables and presented an astrophysical application using data from the Event Horizon Telescope for Sgr A\*. In summary, for the model I,  $\theta_\infty$  displayed a slight deviation from the value found for the Schwarzschild black hole. In contrast, for model II, the effective quantum corrections encapsulated by the parameter  $\xi$  did not influence  $\theta_\infty$ .

As a future direction, exploring particle creation for fermions and bosons, accretion disk of matter, and applying the corrected Newman–Janis technique to obtain an axisymmetric solution are promising topics for further research. These and other related ideas are currently under investigation.

## Acknowledgements

A. A. Araújo Filho is supported by Conselho Nacional de Desenvolvimento Científico e Tecnológico (CNPq) and Fundação de Apoio à Pesquisa do Estado da Paraíba (FAPESQ) - [150891/2023-7]. A. Ö. and R. P. would like to acknowledge networking support of the COST Action CA18108 - Quantum gravity phenomenology in the multi-messenger approach (QG-MM), COST Action CA21106 - COSMIC WISPerS in the Dark Universe: Theory, astrophysics and experiments (CosmicWISPerS), the COST Action CA22113 - Fundamental challenges in theoretical physics (THEORY-CHALLENGES), and the COST Action CA21136 - Addressing observational tensions in cosmology with systematics and fundamental physics (CosmoVerse). A. Ö. would also thank TUBITAK and SCOAP3 for their support.

## References

- [1] Cong Zhang, Jerzy Lewandowski, Yongge Ma, and Jinsong Yang. Black holes and covariance in effective quantum gravity. *arXiv preprint arXiv:2407.10168*, 2024.
- [2] Roger Penrose. Gravitational collapse and space-time singularities. *Physical Review Letters*, 14(3):57, 1965.
- [3] Joseph Gerard Polchinski. *String theory, volume I: An introduction to the bosonic string*. Cambridge university press Cambridge, UK, 1998.
- [4] Jan Ambjørn, Jerzy Jurkiewicz, and Renate Loll. Dynamically triangulating lorentzian quantum gravity. *Nuclear Physics B*, 610(1-2):347–382, 2001.
- [5] Abhay Ashtekar, Beverly K Berger, James Isenberg, and Malcolm MacCallum. *General relativity and gravitation: a centennial perspective*. Cambridge University Press, 2015.
- [6] Sumati Surya. The causal set approach to quantum gravity. *Living Reviews in Relativity*, 22:1–75, 2019.
- [7] David Lovelock. The four-dimensionality of space and the einstein tensor. *Journal of Mathematical Physics*, 13(6):874–876, 1972.
- [8] Timothy Clifton, Pedro G Ferreira, Antonio Padilla, and Constantinos Skordis. Modified gravity and cosmology. *Physics reports*, 513(1-3):1–189, 2012.

- [9] Shinji Mukohyama and Karim Noui. Minimally modified gravity: a hamiltonian construction. *Journal of Cosmology and Astroparticle Physics*, 2019(07):049, 2019.
- [10] Zhi-Bang Yao, Michele Oliosi, Xian Gao, and Shinji Mukohyama. Minimally modified gravity with an auxiliary constraint: A hamiltonian construction. *Physical Review D*, 103(2):024032, 2021.
- [11] Emmanuele Battista. Quantum schwarzschild geometry in effective field theory models of gravity. *Physical Review D*, 109(2):026004, 2024.
- [12] John F Donoghue. Quantum general relativity and effective field theory. In *Handbook of Quantum Gravity*, pages 1–24. Springer, 2023.
- [13] Martin Bojowald and George M Paily. Deformed general relativity and effective actions from loop quantum gravity. *Physical Review D—Particles, Fields, Gravitation, and Cosmology*, 86(10):104018, 2012.
- [14] Rakesh Tibrewala. Inhomogeneities, loop quantum gravity corrections, constraint algebra and general covariance. *Classical and Quantum Gravity*, 31(5):055010, 2014.
- [15] Martin Bojowald, Suddhasattwa Brahma, and Juan D Reyes. Covariance in models of loop quantum gravity: Spherical symmetry. *Physical Review D*, 92(4):045043, 2015.
- [16] Jian-Pin Wu, Martin Bojowald, and Yongge Ma. Anomaly freedom in perturbative models of euclidean loop quantum gravity. *Physical Review D*, 98(10):106009, 2018.
- [17] Abhay Ashtekar, Javier Olmedo, and Parampreet Singh. Quantum transfiguration of kruskal black holes. *Physical review letters*, 121(24):241301, 2018.
- [18] Martin Bojowald. No-go result for covariance in models of loop quantum gravity. *Physical Review D*, 102(4):046006, 2020.
- [19] Muxin Han and Hongguang Liu. Covariant  $\mu^-$ -scheme effective dynamics, mimetic gravity, and nonsingular black holes: Applications to spherically symmetric quantum gravity. *Physical Review D*, 109(8):084033, 2024.
- [20] Rodolfo Gambini, Javier Olmedo, and Jorge Pullin. Towards a quantum notion of covariance in spherically symmetric loop quantum gravity. *Physical Review D*, 105(2):026017, 2022.
- [21] Martin Bojowald. Comment on “towards a quantum notion of covariance in spherically symmetric loop quantum gravity”. *Physical Review D*, 105(10):108901, 2022.
- [22] Abhay Ashtekar, Javier Olmedo, and Parampreet Singh. Regular black holes from loop quantum gravity. In *Regular Black Holes: Towards a New Paradigm of Gravitational Collapse*, pages 235–282. Springer, 2023.
- [23] Kristina Giesel, Hongguang Liu, Parampreet Singh, and Stefan Andreas Weigl. Generalized analysis of a dust collapse in effective loop quantum gravity: fate of shocks and covariance. *arXiv preprint arXiv:2308.10953*, 2023.
- [24] Martin Bojowald and Erick I Duque. Inequivalence of mimetic gravity with models of loop quantum gravity. *Physical Review D*, 109(8):084044, 2024.
- [25] Abhay Ashtekar, Tomasz Pawłowski, and Parampreet Singh. Quantum nature of the big bang. *Physical review letters*, 96(14):141301, 2006.

- [26] Rodolfo Gambini and Jorge Pullin. Black holes in loop quantum gravity: the complete space-time. *Physical review letters*, 101(16):161301, 2008.
- [27] Rodolfo Gambini, Javier Olmedo, and Jorge Pullin. Quantum black holes in loop quantum gravity. *Classical and Quantum Gravity*, 31(9):095009, 2014.
- [28] Abhay Ashtekar, Javier Olmedo, and Parampreet Singh. Quantum transfiguration of kruskal black holes. *Physical review letters*, 121(24):241301, 2018.
- [29] Cong Zhang, Yongge Ma, Shupeng Song, and Xiangdong Zhang. Loop quantum schwarzschild interior and black hole remnant. *Physical Review D*, 102(4):041502, 2020.
- [30] Viqar Husain, Jarod George Kelly, Robert Santacruz, and Edward Wilson-Ewing. Quantum gravity of dust collapse: shock waves from black holes. *Physical Review Letters*, 128(12):121301, 2022.
- [31] Asier Alonso-Bardaji, David Brizuela, and Raúl Vera. An effective model for the quantum schwarzschild black hole. *Physics Letters B*, 829:137075, 2022.
- [32] Cong Zhang, Yongge Ma, Shupeng Song, and Xiangdong Zhang. Loop quantum de-parametrized schwarzschild interior and discrete black hole mass. *Physical Review D*, 105(2):024069, 2022.
- [33] Rodolfo Gambini, Javier Olmedo, and Jorge Pullin. Quantum geometry and black holes. In *Handbook of Quantum Gravity*, pages 1–34. Springer, 2023.
- [34] Viqar Husain, Jarod George Kelly, Robert Santacruz, and Edward Wilson-Ewing. Fate of quantum black holes. *Physical Review D*, 106(2):024014, 2022.
- [35] Asier Alonso-Bardaji, David Brizuela, and Raúl Vera. Nonsingular spherically symmetric black-hole model with holonomy corrections. *Physical Review D*, 106(2):024035, 2022.
- [36] Kristina Giesel, Hongguang Liu, Eric Rullit, Parampreet Singh, and Stefan Andreas Weigl. Embedding generalized ltb models in polymerized spherically symmetric spacetimes. *arXiv preprint arXiv:2308.10949*, 2023.
- [37] Beatriz Elizaga Navascués, Guillermo A Mena Marugán, and Andrés Mínguez-Sánchez. Extended phase space quantization of a black hole interior model in loop quantum cosmology. *Physical Review D*, 108(10):106001, 2023.
- [38] Martin Bojowald and Erick I Duque. Emergent modified gravity coupled to scalar matter. *Physical Review D*, 109(8):084006, 2024.
- [39] Martin Bojowald, Erick I Duque, and Dennis Hartmann. New type of large-scale signature change in emergent modified gravity. *Physical Review D*, 109(8):084001, 2024.
- [40] Shulan Li and Jian-Pin Wu. Gravitational waves with generalized holonomy corrections. *The European Physical Journal C*, 84(6):629, 2024.
- [41] Asier Alonso-Bardaji and David Brizuela. Spacetime geometry from canonical spherical gravity. *Physical Review D*, 109(4):044065, 2024.
- [42] Cong Zhang. Reduced phase space quantization of black holes: Path integrals and effective dynamics. *Physical Review D*, 104(12):126003, 2021.

- [43] Benjamin P Abbott, Richard Abbott, TD Abbott, F Acernese, K Ackley, C Adams, T Adams, P Addresso, Rana X Adhikari, Vaishali B Adya, et al. Gw170814: a three-detector observation of gravitational waves from a binary black hole coalescence. *Phys. Rev. Lett.*, 119(14):141101, 2017.
- [44] B Abbott, S Jawahar, N Lockerbie, and K Tokmakov. Ligo scientific collaboration and virgo collaboration (2016) directly comparing gw150914 with numerical solutions of einstein’s equations for binary black hole coalescence. *Phys. Rev. D*, 94:064035, 2016.
- [45] Benjamin P Abbott, R Abbott, TD Abbott, MR Abernathy, Fausto Acernese, K Ackley, C Adams, T Adams, Paolo Addresso, RX Adhikari, et al. Gw151226: observation of gravitational waves from a 22-solar-mass binary black hole coalescence. *Phys. Rev. Lett.*, 116(24):241103, 2016.
- [46] N Heidari, H Hassanabadi, A. A Araújo Filho, J Kriz, S Zare, and P. J Porfírio. Gravitational signatures of a non-commutative stable black hole. *Physics of the Dark Universe*, page 101382, 2023.
- [47] Suvodip Mukherjee, Benjamin D Wandelt, and Joseph Silk. Probing the theory of gravity with gravitational lensing of gravitational waves and galaxy surveys. *Monthly Notices of the Royal Astronomical Society*, 494(2):1956–1970, 2020.
- [48] A. A Araújo Filho, H Hassanabadi, N Heidari, J Kríz, and S Zare. Gravitational traces of bumblebee gravity in metric–affine formalism. *Classical and Quantum Gravity*, 41(5):055003, 2024.
- [49] O Contigiani. Lensing efficiency for gravitational wave mergers. *Monthly Notices of the Royal Astronomical Society*, 492(3):3359–3363, 2020.
- [50] A. A Araújo Filho. Implications of a simpson–visser solution in verlinde’s framework. *The European Physical Journal C*, 84(1):1–22, 2024.
- [51] A. A Araújo Filho. Analysis of a regular black hole in verlinde’s gravity. *Classical and Quantum Gravity*, 41(1):015003, 2023.
- [52] Charles Galton Darwin. The gravity field of a particle. *Proceedings of the Royal Society of London. Series A. Mathematical and Physical Sciences*, 249(1257):180–194, 1959.
- [53] Robert d’Escourt Atkinson. On light tracks near a very massive star. *Astronomical Journal*, Vol. 70, p. 517, 70:517, 1965.
- [54] C. T. Cunningham and James M. Bardeen. The Optical Appearance of a Star Orbiting an Extreme Kerr Black Hole. *The Astrophysical Journal*, 183:237–264, July 1973.
- [55] Heino Falcke, Fulvio Melia, and Eric Agol. Viewing the shadow of the black hole at the galactic center. *Astrophys. J. Lett.*, 528:L13, 2000.
- [56] Sunny Vagnozzi and Luca Visinelli. Hunting for extra dimensions in the shadow of M87\*. *Phys. Rev. D*, 100(2):024020, 2019.
- [57] Cosimo Bambi, Katherine Freese, Sunny Vagnozzi, and Luca Visinelli. Testing the rotational nature of the supermassive object M87\* from the circularity and size of its first image. *Phys. Rev. D*, 100(4):044057, 2019.

- [58] Alireza Allahyari, Mohsen Khodadi, Sunny Vagnozzi, and David F. Mota. Magnetically charged black holes from non-linear electrodynamics and the Event Horizon Telescope. *JCAP*, 02:003, 2020.
- [59] Rahul Kumar, Sushant G. Ghosh, and Anzhong Wang. Gravitational deflection of light and shadow cast by rotating Kalb-Ramond black holes. *Phys. Rev. D*, 101(10):104001, 2020.
- [60] Misba Afrin, Rahul Kumar, and Sushant G. Ghosh. Parameter estimation of hairy Kerr black holes from its shadow and constraints from M87\*. *Mon. Not. Roy. Astron. Soc.*, 504:5927–5940, 2021.
- [61] Mohsen Khodadi, Gaetano Lambiase, and David F. Mota. No-hair theorem in the wake of Event Horizon Telescope. *JCAP*, 09:028, 2021.
- [62] Misba Afrin and Sushant G. Ghosh. Testing Horndeski Gravity from EHT Observational Results for Rotating Black Holes. *Astrophys. J.*, 932(1):51, 2022.
- [63] Mohsen Khodadi and Gaetano Lambiase. Probing Lorentz symmetry violation using the first image of Sagittarius A\*: Constraints on standard-model extension coefficients. *Phys. Rev. D*, 106(10):104050, 2022.
- [64] Qi-Ming Fu and Xin Zhang. Gravitational lensing by a black hole in effective loop quantum gravity. *Phys. Rev. D*, 105(6):064020, 2022.
- [65] Misba Afrin, Sunny Vagnozzi, and Sushant G. Ghosh. Tests of Loop Quantum Gravity from the Event Horizon Telescope Results of Sgr A\*. *Astrophys. J.*, 944(2):149, 2023.
- [66] Misba Afrin and Sushant G. Ghosh. EHT observables as a tool to estimate parameters of supermassive black holes. *Mon. Not. Roy. Astron. Soc.*, 524(3):3683–3691, 2023.
- [67] Sushant G. Ghosh and Misba Afrin. An Upper Limit on the Charge of the Black Hole Sgr A\* from EHT Observations. *Astrophys. J.*, 944(2):174, 2023.
- [68] Misba Afrin, Sushant G. Ghosh, and Anzhong Wang. Testing EGB gravity coupled to bumblebee field and black hole parameter estimation with EHT observations. *Phys. Dark Univ.*, 46:101642, 2024.
- [69] Mohsen Khodadi, Sunny Vagnozzi, and Javad T. Firouzjaee. Event Horizon Telescope observations exclude compact objects in baseline mimetic gravity. *Sci. Rep.*, 14(1):26932, 2024.
- [70] Kazunori Akiyama et al. First M87 Event Horizon Telescope Results. VI. The Shadow and Mass of the Central Black Hole. *Astrophys. J. Lett.*, 875(1):L6, 2019.
- [71] Kazunori Akiyama, Antxon Alberdi, Walter Alef, Keiichi Asada, Rebecca Azulay, Anne-Kathrin Baczko, David Ball, Mislav Baloković, John Barrett, Dan Bintley, et al. First m87 event horizon telescope results. v. physical origin of the asymmetric ring. *The Astrophysical Journal Letters*, 875(1):L5, 2019.
- [72] Kazunori Akiyama, Antxon Alberdi, Walter Alef, Keiichi Asada, Rebecca Azulay, Anne-Kathrin Baczko, David Ball, Mislav Baloković, John Barrett, Dan Bintley, et al. First m87 event horizon telescope results. ii. array and instrumentation. *The Astrophysical Journal Letters*, 875(1):L2, 2019.
- [73] Event Horizon Telescope Collaboration et al. First m87 event horizon telescope results. iv. imaging the central supermassive black hole. *arXiv preprint arXiv:1906.11241*, 2019.



- [74] Event Horizon Telescope Collaboration et al. First m87 event horizon telescope results. iv. imaging the central supermassive black hole. *arXiv preprint arXiv:1906.11241*, 2019.
- [75] Kazunori Akiyama, Antxon Alberdi, Walter Alef, Keiichi Asada, Rebecca Azulay, Anne-Kathrin Baczko, David Ball, Mislav Baloković, John Barrett, Dan Bintley, et al. First m87 event horizon telescope results. v. physical origin of the asymmetric ring. *The Astrophysical Journal Letters*, 875(1):L5, 2019.
- [76] Volker Perlick. Theoretical gravitational lensing—beyond the weak-field small-angle approximation. In *The Eleventh Marcel Grossmann Meeting: On Recent Developments in Theoretical and Experimental General Relativity, Gravitation and Relativistic Field Theories (In 3 Volumes)*, pages 680–699. World Scientific, 2008.
- [77] Kumar Shwetketu Virbhadra and George FR Ellis. Schwarzschild black hole lensing. *Physical Review D*, 62(8):084003, 2000.
- [78] Simonetta Frittelli, Thomas P Kling, and Ezra T Newman. Spacetime perspective of schwarzschild lensing. *Phys. Rev. D*, 61(6):064021, 2000.
- [79] Valerio Bozza, Salvatore Capozziello, Gerardo Iovane, and Gaetano Scarpetta. Strong field limit of black hole gravitational lensing. *General Relativity and Gravitation*, 33:1535–1548, 2001.
- [80] Naoki Tsukamoto. Deflection angle in the strong deflection limit in a general asymptotically flat, static, spherically symmetric spacetime. *Phys. Rev. D*, 95(6):064035, 2017.
- [81] K. S. Virbhadra. Compactness of supermassive dark objects at galactic centers. *Can. J. Phys.*, 102:512, 2024.
- [82] Margherita Grespan and Marek Biesiada. Strong gravitational lensing of gravitational waves: A review. *Universe*, 9(5):200, 2023.
- [83] Pedro VP Cunha and Carlos AR Herdeiro. Shadows and strong gravitational lensing: a brief review. *General Relativity and Gravitation*, 50:1–27, 2018.
- [84] Xiao-Mei Kuang and Ali Övgün. Strong gravitational lensing and shadow constraint from M87\* of slowly rotating Kerr-like black hole. *Annals Phys.*, 447:169147, 2022.
- [85] R Benton Metcalf, MASSIMO Meneghetti, Camille Avestruz, Fabio Bellagamba, Clécio R Bom, Emmanuel Bertin, Rémi Cabanac, F Courbin, Andrew Davies, Etienne Decencière, et al. The strong gravitational lens finding challenge. *Astronomy & Astrophysics*, 625:A119, 2019.
- [86] Ali Övgün, İzzet Sakallı, and Joel Saavedra. Shadow cast and Deflection angle of Kerr-Newman-Kasuya spacetime. *JCAP*, 10:041, 2018.
- [87] Kumar S Virbhadra and George FR Ellis. Gravitational lensing by naked singularities. *Physical Review D*, 65(10):103004, 2002.
- [88] Gennady S Bisnovatyi-Kogan and Oleg Yu Tsupko. Gravitational lensing in presence of plasma: strong lens systems, black hole lensing and shadow. *Universe*, 3(3):57, 2017.
- [89] A. A Araújo Filho. Antisymmetric tensor influence on charged black hole lensing phenomena and time delay. *arXiv preprint arXiv:2406.11582*, 2024.

- [90] Jose María Ezquiaga, Daniel E Holz, Wayne Hu, Macarena Lagos, and Robert M Wald. Phase effects from strong gravitational lensing of gravitational waves. *Physical Review D*, 103(6):064047, 2021.
- [91] KS Virbhadra, D Narasimha, and SM Chitre. Role of the scalar field in gravitational lensing. *arXiv preprint astro-ph/9801174*, 1998.
- [92] Mert Okyay and Ali Övgün. Nonlinear electrodynamics effects on the black hole shadow, deflection angle, quasinormal modes and greybody factors. *JCAP*, 01(01):009, 2022.
- [93] Zonghai Li and Ali Övgün. Finite-distance gravitational deflection of massive particles by a Kerr-like black hole in the bumblebee gravity model. *Phys. Rev. D*, 101(2):024040, 2020.
- [94] Ali Övgün. Light deflection by Damour-Solodukhin wormholes and Gauss-Bonnet theorem. *Phys. Rev. D*, 98(4):044033, 2018.
- [95] Reggie C. Pantig, Leonardo Mastrototaro, Gaetano Lambiase, and Ali Övgün. Shadow, lensing, quasinormal modes, greybody bounds and neutrino propagation by dyonic ModMax black holes. *Eur. Phys. J. C*, 82(12):1155, 2022.
- [96] Reggie C. Pantig and Ali Övgün. Testing dynamical torsion effects on the charged black hole’s shadow, deflection angle and greybody with M87\* and Sgr. A\* from EHT. *Annals Phys.*, 448:169197, 2023.
- [97] Masamune Oguri. Strong gravitational lensing of explosive transients. *Reports on Progress in Physics*, 82(12):126901, 2019.
- [98] A. A Araújo Filho, J. R Nascimento, A. Yu Petrov, and P. J Porfírio. Gravitational lensing by a lorentz-violating black hole. *arXiv preprint arXiv:2404.04176*, 2024.
- [99] Sumanta Chakraborty and Soumitra SenGupta. Strong gravitational lensing—a probe for extra dimensions and kalb-ramond field. *Journal of Cosmology and Astroparticle Physics*, 2017(07):045, 2017.
- [100] Rajibul Shaikh and Sayan Kar. Gravitational lensing by scalar-tensor wormholes and the energy conditions. *Phys. Rev. D*, 96(4):044037, 2017.
- [101] Rajibul Shaikh, Pritam Banerjee, Suvankar Paul, and Tapobrata Sarkar. Strong gravitational lensing by wormholes. *JCAP*, 2019(07):028, 2019.
- [102] Ali Övgün, Kimet Jusufi, and İzzet Sakallı. Exact traversable wormhole solution in bumblebee gravity. *Physical Review D*, 99(2):024042, 2019.
- [103] Gary W Gibbons and Martin Vyska. The application of weierstrass elliptic functions to schwarzschild null geodesics. *Class. Quant. Grav.*, 29(6):065016, 2012.
- [104] Naoki Tsukamoto, Tomohiro Harada, and Kohji Yajima. Can we distinguish between black holes and wormholes by their einstein-ring systems? *Phys. Rev. D*, 86(10):104062, 2012.
- [105] Naoki Tsukamoto. Retrolensing by a wormhole at deflection angles  $\pi$  and  $3\pi$ . *Phys. Rev. D*, 95(8):084021, 2017.
- [106] Naoki Tsukamoto. Strong deflection limit analysis and gravitational lensing of an ellis wormhole. *Phys. Rev. D*, 94(12):124001, 2016.

- [107] Naoki Tsukamoto, Yungui Gong, et al. Retrolensing by a charged black hole. *Phys. Rev. D*, 95(6):064034, 2017.
- [108] Ernesto F Eiroa, Gustavo E Romero, and Diego F Torres. Reissner-nordström black hole lensing. *Physical Review D*, 66(2):024010, 2002.
- [109] Ernesto F Eiroa and Diego F Torres. Strong field limit analysis of gravitational retrolensing. *Phys. Rev. D*, 69(6):063004, 2004.
- [110] Kimet Jusufi and Ali Övgün. Gravitational lensing by rotating wormholes. *Physical Review D*, 97(2):024042, 2018.
- [111] Tien Hsieh, Da-Shin Lee, and Chi-Yong Lin. Strong gravitational lensing by kerr and kerr-newman black holes. *Physical Review D*, 103(10):104063, 2021.
- [112] Valerio Bozza, Fabiana De Luca, Gaetano Scarpetta, and M Sereno. Analytic kerr black hole lensing for equatorial observers in the strong deflection limit. *Phys. Rev. D*, 72(8):083003, 2005.
- [113] Samuel E Vazquez and Ernesto P Esteban. Strong field gravitational lensing by a kerr black hole. *arXiv preprint gr-qc/0308023*, 2003.
- [114] Tien Hsieh, Da-Shin Lee, and Chi-Yong Lin. Gravitational time delay effects by kerr and kerr-newman black holes in strong field limits. *Physical Review D*, 104(10):104013, 2021.
- [115] Amir B Aazami, Charles R Keeton, and AO Petters. Lensing by kerr black holes. ii: Analytical study of quasi-equatorial lensing observables. *J. Math. Phys.*, 52(10), 2011.
- [116] Valerio Bozza. Quasiequatorial gravitational lensing by spinning black holes in the strong field limit. *Physical Review D*, 67(10):103006, 2003.
- [117] Valerio Bozza and Gaetano Scarpetta. Strong deflection limit of black hole gravitational lensing with arbitrary source distances. *Phys. Rev. D*, 76(8):083008, 2007.
- [118] Valerio Bozza, Fabiana De Luca, and Gaetano Scarpetta. Kerr black hole lensing for generic observers in the strong deflection limit. *Phys. Rev. D*, 74(6):063001, 2006.
- [119] KS Virbhadra. Distortions of images of schwarzschild lensing. *Physical Review D*, 106(6):064038, 2022.
- [120] KS Virbhadra. Conservation of distortion of gravitationally lensed images. *Physical Review D*, 109(12):124004, 2024.
- [121] Haida Li and Xiangdong Zhang. Gravitational Lensing Effects from Models of Loop Quantum Gravity with Rigorous Quantum Parameters, 9 2024.
- [122] Hao Liu, Meng-Yun Lai, Xiao-Yin Pan, Hyat Huang, and De-Cheng Zou. Gravitational lensing effect of black holes in effective quantum gravity. *arXiv preprint arXiv:2408.11603*, 2024.
- [123] Valerio Bozza. Gravitational lensing in the strong field limit. *Physical Review D*, 66(10):103001, 2002.
- [124] Wentao Liu, Di Wu, and Jieci Wang. Light rings and shadows of static black holes in effective quantum gravity. *arXiv preprint arXiv:2408.05569*, 2024.
- [125] Zainab Malik. Perturbations and quasinormal modes of the dirac field in effective quantum gravity. *arXiv preprint arXiv:2409.01561*, 2024.

- [126] RA Konoplya and OS Stashko. Probing the effective quantum gravity via quasinormal modes and shadows of black holes. *arXiv preprint arXiv:2408.02578*, 2024.
- [127] Sergey Bolokhov. Long lived quasinormal modes in the effective quantum gravity, 2024.
- [128] Zainab Malik. Quasinormal Modes and the Hod’s Bound in the Effective Quantum Gravity, 2024.
- [129] GW Gibbons and MC Werner. Applications of the gauss–bonnet theorem to gravitational lensing. *Classical and Quantum Gravity*, 25(23):235009, 2008.
- [130] Naoki Tsukamoto. Deflection angle in the strong deflection limit in a general asymptotically flat, static, spherically symmetric spacetime. *Phys. Rev. D*, 95(6):064035, 2017.
- [131] J. A. V Campos, M. A Anacleto, F. A Brito, and E Passos. Quasinormal modes and shadow of noncommutative black hole. *Scientific Reports*, 12(1):8516, 2022.
- [132] Marcos A Anacleto, J. A. V Campos, Francisco A Brito, and E Passos. Quasinormal modes and shadow of a schwarzschild black hole with gup. *Annals of Physics*, 434:168662, 2021.
- [133] Caio FB Macedo, Ednilton S de Oliveira, and Luís CB Crispino. Scattering by regular black holes: planar massless scalar waves impinging upon a bardeen black hole. *Physical Review D*, 92(2):024012, 2015.
- [134] Caio FB Macedo, Luiz CS Leite, and Luís CB Crispino. Absorption by dirty black holes: Null geodesics and scalar waves. *Physical Review D*, 93(2):024027, 2016.
- [135] MA Anacleto, FA Brito, JAV Campos, and E Passos. Absorption, scattering and shadow by a noncommutative black hole with global monopole. *The European Physical Journal C*, 83(4):298, 2023.
- [136] Caio FB Macedo, Luiz CS Leite, Ednilton S Oliveira, Sam R Dolan, and Luis CB Crispino. Absorption of planar massless scalar waves by kerr black holes. *Physical Review D*, 88(6):064033, 2013.
- [137] Sam R Dolan, Ednilton S Oliveira, and Luís CB Crispino. Scattering of sound waves by a canonical acoustic hole. *Physical Review D*, 79(6):064014, 2009.
- [138] Luís CB Crispino, Sam R Dolan, and Ednilton S Oliveira. Scattering of massless scalar waves by reissner-nordström black holes. *Physical Review D*, 79(6):064022, 2009.
- [139] Luis CB Crispino, Atsushi Higuchi, Ednilton S Oliveira, and Jorge V Rocha. Greybody factors for nonminimally coupled scalar fields in schwarzschild–de sitter spacetime. *Physical Review D*, 87(10):104034, 2013.
- [140] Sumit R. Das, Gary W. Gibbons, and Samir D. Mathur. Universality of low-energy absorption cross-sections for black holes. *Phys. Rev. Lett.*, 78:417–419, 1997.
- [141] Atsushi Higuchi. Low frequency scalar absorption cross-sections for stationary black holes. *Class. Quant. Grav.*, 18:L139, 2001. [Addendum: *Class.Quant.Grav.* 19, 599 (2002)].
- [142] Luiz CS Leite, Carolina L Benone, and Luís CB Crispino. Scalar absorption by charged rotating black holes. *Physical Review D*, 96(4):044043, 2017.

- [143] İzzet Sakalli and Sara Kanzi. Topical review: greybody factors and quasinormal modes for black holes in various theories—fingerprints of invisibles. *Turkish Journal of Physics*, 46(2):51–103, 2022.
- [144] P Boonserm, T Ngampitipan, and Pitayuth Wongjun. Greybody factor for black string in dRGT massive gravity. *The European Physical Journal C*, 79:1–9, 2019.
- [145] Ali Övgün, Reggie C Pantig, and Ángel Rincón. Shadow and greybody bounding of a regular scale-dependent black hole solution. *Annals of Physics*, 463:169625, 2024.
- [146] Ahmad Al-Badawi, Sohan Kumar Jha, and Anisur Rahaman. The fermionic greybody factor and quasinormal modes of hairy black holes, as well as hawking radiation’s power spectrum and sparsity. *The European Physical Journal C*, 84(2):145, 2024.
- [147] Petarpa Boonserm and Matt Visser. Transmission probabilities and the miller–good transformation. *Journal of Physics A: Mathematical and Theoretical*, 42(4):045301, 2008.
- [148] A. A Araújo Filho, J. A. A. S Reis, and H Hassanabadi. Exploring antisymmetric tensor effects on black hole shadows and quasinormal frequencies. *Journal of Cosmology and Astroparticle Physics*, 2024(05):029, 2024.
- [149] N Heidari, JAAS Reis, H Hassanabadi, et al. The impact of an antisymmetric tensor on charged black holes: evaporation process, geodesics, deflection angle, scattering effects and quasinormal modes. *arXiv preprint arXiv:2404.10721*, 2024.
- [150] Narges Heidari, Hassan Hassanabadi, A. A Araújo Filho, and John Kriz. Exploring non-commutativity as a perturbation in the schwarzschild black hole: quasinormal modes, scattering, and shadows. *The European Physical Journal C*, 84(6):566, 2024.
- [151] N Heidari, Caio F. B Macedo, H Hassanabadi, et al. Scattering effects of bumblebee gravity in metric affine formalism. *arXiv preprint arXiv:2407.05321*, 2024.
- [152] F Hosseinifar, MY Zhang, H Chen, H Hassanabadi, et al. Shadows, greybody factors, emission rate, topological charge, and phase transitions for a charged black hole with a kalb-ramond field background. *arXiv preprint arXiv:2407.07017*, 2024.
- [153] H Chen, MY Zhang, F Hosseinifar, H Hassanabadi, et al. Thermal, topological, and scattering effects of an ads charged black hole with an antisymmetric tensor background. *arXiv preprint arXiv:2408.03090*, 2024.
- [154] Ezra Newman and Roger Penrose. An approach to gravitational radiation by a method of spin coefficients. *Journal of Mathematical Physics*, 3(3):566–578, 1962.
- [155] Subrahmanijan Chandrasekhar. The mathematical theory of black holes. In *General Relativity and Gravitation: Invited Papers and Discussion Reports of the 10th International Conference on General Relativity and Gravitation, Padua, July 3–8, 1983*, pages 5–26. Springer, 1984.
- [156] Saulo Albuquerque, Iarley P Lobo, and Valdir B Bezerra. Massless dirac perturbations in a consistent model of loop quantum gravity black hole: quasinormal modes and particle emission rates. *Classical and Quantum Gravity*, 40(17):174001, 2023.
- [157] Ahmad Al-Badawi and Sohan Kumar Jha. Massless dirac perturbations of black holes in f (q) gravity: quasinormal modes and a weak deflection angle. *Communications in Theoretical Physics*, 76(9):095403, 2024.

- [158] Alexandre Arbey, Jérémy Auffinger, Marc Geiller, Etera R Livine, and Francesco Sartini. Hawking radiation by spherically-symmetric static black holes for all spins: Teukolsky equations and potentials. *Physical Review D*, 103(10):104010, 2021.
- [159] Saraswati Devi, Rittick Roy, and Sayan Chakrabarti. Quasinormal modes and greybody factors of the novel four dimensional gauss–bonnet black holes in asymptotically de sitter space time: scalar, electromagnetic and dirac perturbations. *The European Physical Journal C*, 80(8):760, 2020.
- [160] Clarissa-Marie Claudel, K. S. Virbhadra, and G. F. R. Ellis. The Geometry of photon surfaces. *J. Math. Phys.*, 42:818–838, 2001.
- [161] K. S. Virbhadra and G. F. R. Ellis. Gravitational lensing by naked singularities. *Phys. Rev. D*, 65:103004, 2002.
- [162] R. A. Konoplya and O. S. Stashko. Probing the Effective Quantum Gravity via Quasinormal Modes and Shadows of Black Holes, 8 2024.
- [163] Sunny Vagnozzi et al. Horizon-scale tests of gravity theories and fundamental physics from the Event Horizon Telescope image of Sagittarius A. *Class. Quant. Grav.*, 40(16):165007, 2023.
- [164] Prashant Kocherlakota et al. Constraints on black-hole charges with the 2017 EHT observations of M87\*. *Phys. Rev. D*, 103(10):104047, 2021.
- [165] Hao Liu, Meng-Yun Lai, Xiao-Yin Pan, Hyat Huang, and De-Cheng Zou. Gravitational lensing effect of black holes in effective quantum gravity. *arXiv preprint arXiv:2408.11603*, 2024.
- [166] G. W. Gibbons and M. C. Werner. Applications of the Gauss-Bonnet theorem to gravitational lensing. *Class. Quant. Grav.*, 25:235009, 2008.
- [167] Zonghai Li, Guodong Zhang, and Ali Övgün. Circular Orbit of a Particle and Weak Gravitational Lensing. *Phys. Rev. D*, 101(12):124058, 2020.
- [168] Wolfgang Hasse and Volker Perlick. Gravitational lensing in spherically symmetric static spacetimes with centrifugal force reversal. *General Relativity and Gravitation*, 34:415–433, 2002.
- [169] Valerio Bozza, Salvatore Capozziello, Gerardo Iovane, and Gaetano Scarpetta. Strong field limit of black hole gravitational lensing. *General Relativity and Gravitation*, 33:1535–1548, 2001.
- [170] Rahul Kumar, Shafqat Ul Islam, and Sushant G Ghosh. Gravitational lensing by charged black hole in regularized 4 d einstein–gauss–bonnet gravity. *The European Physical Journal C*, 80(12):1128, 2020.
- [171] Reinhard Genzel, Frank Eisenhauer, and Stefan Gillessen. The galactic center massive black hole and nuclear star cluster. *Reviews of modern physics*, 82(4):3121–3195, 2010.
- [172] Kazunori Akiyama, Antxon Alberdi, Walter Alef, Juan Carlos Algaba, Richard Anantua, Keiichi Asada, Rebecca Azulay, Uwe Bach, Anne-Kathrin Baczko, David Ball, et al. First sagittarius a\* event horizon telescope results. vi. testing the black hole metric. *The Astrophysical Journal Letters*, 930(2):L17, 2022.